RESEARCH ARTICLE

Key Points:
- Numerical results show that a low-viscosity crustal layer (LVCL) determines the width of highly thinned crust and crustal thermal distribution
- Variation in the LVCL thickness may be a mechanism for the differential stretching and thermal characteristics along strike of the northern SCS margin
- Ultra-thinning upper crust develops when the SCS continent breaks apart

Supporting Information:
- Supporting Information S1

Correspondence to:
F. Li and Z. Sun
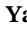iamlifucheng@163.com; zhensun@sc-sio.ac.cn

Low-Viscosity Crustal Layer Controls the Crustal Architecture and Thermal Distribution at Hyperextended Margins: Modeling Insight and Application to the Northern South China Sea Margin

Fucheng Li[1] , **Zhen Sun[1]** , **Xiong Pang[2]**, **Jie Liao[3]** , **Hongfeng Yang[4]** , **Hui Xie[5]** , **Haiteng Zhuo[1]**, and **Zhongxian Zhao[1]**

[1]CAS Key Laboratory of Ocean and Marginal Sea Geology, South China Sea Institute of Oceanology, Guangzhou, China, [2]China National Offshore Oil Corporation Ltd-Shenzhen/China National Offshore Oil Corporation Ltd-Deepwater, Shenzhen, China, [3]School of Earth Sciences and Engineering, Sun Yat-Sen University, Guangzhou, China, [4]Earth System Science Programme, Faculty of Science, The Chinese University of Hong Kong, Hong Kong, [5]Guangdong Province Key Laboratory for Coastal Ocean Variation and Disaster Prediction, Guangdong Ocean University, Zhanjiang, China

Abstract A low-viscosity crustal layer (LVCL) due to partial melt and/or hydration has been detected within the continental crust (e.g., in South China block), but its role in the development of hyperextended margins is still not entirely understood. Using 2-D thermomechanical modeling, we simulate the lithospheric extension with a LVCL embedded within the continental crust. Results show that the ductile layer determines the width of highly thinned crust and the crustal thermal distribution. Detailed effects are found by varying the initial effective viscosity and thickness of the layer: (1) a rheologically weaker and/or thicker LVCL accommodates more deformation and thus results in a slow and distributed crustal thinning and (2) preferential removal of the lithospheric mantle places the crust in direct contact with the hot upwelling asthenosphere, promoting the development of highly thinned and hot continental crust. Both the widths of highly thinned crust and the thermal values increase when the rheology of the ductile layer decreases or the thickness increases. Furthermore, we obtain the crustal thickness and geothermal characteristics of the northern South China Sea (SCS) margin using reprocessed geophysical data and newly complied heat flow data. A detailed comparison of our modeling results with the northern SCS margin suggests that variation in the LVCL thickness may be a possible mechanism for the differential width of highly thinned crust and high heat flow zone along strike of the northern SCS margin.

1. Introduction

Rifted margins form through lithospheric stretching, thinning, and eventual breakup. As rifting proceeds, various crustal architectures are developed and may be influenced by several parameters. For example, based on wide-angle seismic data and Ocean Drilling Program drilling results from the West Iberia margin, Dean et al. (2000) concluded that the ocean-continent transition zone is dominantly composed of either exposed upper mantle or serpentinized peridotite. Similar serpentinized mantle also has been found in the southeastern Canadian margin (Lau et al., 2018) and Porcupine Basin (Prada et al., 2017). Upper mantle exhumes when the crust ruptures before the lower lithosphere during rifting (Huismans & Beaumont, 2014), and the serpentinized peridotite is considered to be affected by extension velocity and lower crustal strength that control onset of melting and serpentinization (Pérez-Gussinyé et al., 2006; Ros et al., 2017).

The rifted margin also exhibits a broad zone of highly extended continental crust that varies in widths (Contrucci et al., 2004; Lau et al., 2006). It is generally accepted that the initial effective lithospheric strength (particularly the lower crustal rheology) and divergent rate determine the width and duration of continental rifting (e.g., Brune et al., 2017; Burov & Watts, 2006; Chen et al., 2017; Gueydan & Précigout, 2014; Liao & Gerya, 2015; Pérez-Gussinyé et al., 2003). By performing three-dimensional numerical simulations, Le Pourhiet et al. (2018) have further suggested that oceanic propagators play an equal or even greater role in the width of the rifted margin. In addition, crustal thickness and lithospheric thermal structure also determine the width of highly extended continental crust (e.g., Svartman Dias et al., 2015; Tetreault & Buiter,
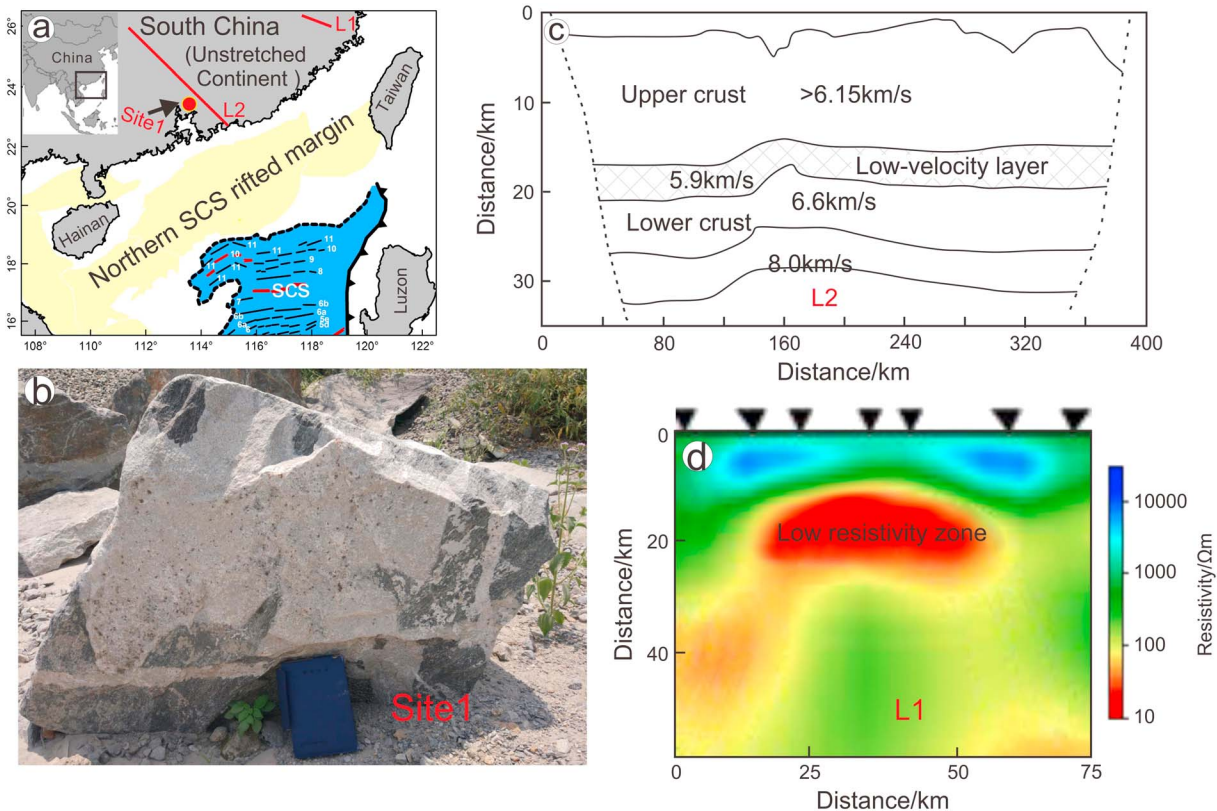
Figure 1. Geological and geophysical characteristics of the low-viscosity crustal layer in South China continent's interior. Rocks in Figure 1b are the gneissic granites sampled from the Zengcheng city during our field trip (the book used for scale is 25 cm high and 15 cm wide). These rocks derived from the partial melting of middle crust before the onset of continental extension (Li et al., 2007). Seismic profile (Figure 1c) and resistivity model (Figure 1d) reveal the presence of low-velocity and low-resistivity zone at middle crustal depths (Deng et al., 2011; Hu et al., 2017; Liao et al., 1988; Zhang & Wang, 2007). The locations of the profile and outcrop site are shown in Figure 1a. SCS = South China Sea.

2017). Another important feature of the highly extended crust is large-scale crustal asymmetry in the conjugate margins (e.g., Gerlings et al., 2012). One of the best studied asymmetric rifted margins is the Iberian-Newfoundland, where the continental crust thinning to less than 10 km occurs over distances of 100–200 km at the Iberian distal margin, whereas its conjugate Newfoundland margin has an abrupt crustal thinning over a distance of ~50 km (Hopper et al., 2007; Peron-Pinvidic et al., 2013; Whitmarsh et al., 2001). In order to explain the asymmetry in the conjugate margins, sequential faulting model and rift migration model have been proposed and well compared with the natural examples (Brune et al., 2014; Ranero & Pérez-Gussinyé, 2010).

Recently, a low-viscosity crustal layer (LVCL) lying within the continental crust has been detected by both geophysical and geochemical studies in the south Chinese continent. For example, a layer of lower velocity (~5.5–6.0 km/s) has been recognized in the South China continent's interior (Figure 1b; Liao et al., 1988; Deng et al., 2011, and reference therein). The low-velocity layer is typically 3–6 km thick within the crust and probably results from partial melting during Triassic-Jurassic orogeny in the South China block (Deng et al., 2011; Li et al., 2007). In the Triassic-Jurassic collision zone, material sourced from the subducting plate melts partially and flows toward the lower-elevation via middle crustal flow (Li et al., 2007). As a result, gneissic granites that derived from partial melting are commonly outcropped in the South China before the onset of continental extension (Li et al., 2007). Additionally, resistivity model inverted from the magnetotelluric data images a zone of low resistivity (~10 Ωm) at midcrustal depths of the continent (Hu et al., 2017; Figure 1c). Assuming that low resistivity is mainly caused by partial melting, the zone of minimal resistivity of 10 Ωm implies the presence of a rheologically LVCL (Unsworth et al., 2005). Such LVCLs with similar geophysical characteristics but different evolutionary histories also have been found beneath western New Zealand (Klepeis et al., 2007), the Central Range of Taiwan (Kuo-Chen et al., 2012), and the Pamir (Mechie et al., 2012). They are composed of quartz-rich

rocks and characterized by a lower viscosity than its bounding layers, showing geophysical characteristics of low V_P/V_S ratios, compressional seismic wave speed, and high electrical conductivity (e.g., Kendall et al., 2003; Lavier & Manatschal, 2006; Li, Sun, & Zhang, 2018).

Previous studies have investigated the influence of ductile lower crust on the evolution of rifted margins. It may control the level of mechanical coupling between crust and mantle, initially leads to the formation of detachment surface and delays rift propagation during extension (e.g., Allken et al., 2012; Burov & Watts, 2006; Lavier & Manatschal, 2006; Pérez-Gussinyé et al., 2003). However, a heterogeneous crustal structure that a ductile layer embeds in the crust has not been taken into account and, thereby, its roles on the development of hyperextended margin are still unclear (e.g., on the width of highly thinned crust and the crustal thermal distribution).

To address the above-mentioned question, we set up a series of numerical models with and without LVCL embedded within the crust. For convenience, we refer to the model without LVCL as "two-layer-crust model," and the model with LVCL as "three-layer-crust model." To differentiate the evolution of the two-extensional end-members, we compare the major characteristics of these models. Parameter sensitivity analysis also has been performed to investigate how the rheological strength, the thickness of LVCL, and the extension velocity affect the development of rifted margins. In addition, we obtain the crustal thickness and geothermal characteristics of the northern South China Sea (SCS) margin by reprocessing the geophysical data and then compare the numerical results with the northern SCS to explore the dynamics of differential stretching characteristics.

2. Data and Methods

2.1. Geophysical Data Acquisition and Processing

2.1.1. Gravity Modeling and Data Sources

Three-dimensional gravity modeling constrained by refraction data is applied to get a new Moho depth map in the northern SCS area. The gravimetric solutions are based on the forward algorithm given by Parker (1973). The forward algorithm calculates the Fourier transform of the gravitational anomaly as the sum of the Fourier transforms of the powers of the perturbing topography. Oldenburg (1974) further rearranged Parker's expression to calculate the geometry of the density interface from the gravity anomaly rapidly. The method has been already tested using synthetic and field gravity anomaly data. It yielded results and coincided with the known source parameters. In this paper, we use a computer program, which was developed by Gómez-Ortiz and Agarwal (2005) according to the 3-D extension of the Parker-Oldenburg's method, to obtain the Moho depth in the SCS. This program is capable of inverting large volumes of gravity data and has been proven their practicality with field data (Gómez-Ortiz & Agarwal, 2005).

Gravity data are obtained from the satellite-derived gravity field of Sandwell (Sandwell et al., 2014). Bathymetry is taken from the SRTM30 complied by Scripps Institution of Oceanography (Becker et al., 2009). Sediment thickness is from the project of Total Sediment Thickness of the World's Oceans and Marginal Seas, which is updated by the National Oceanic and Atmospheric Administration National Geophysical Data Center (Whittaker et al., 2013).

2.1.2. Heat Flow Data

Heat flow data are direct evidence for understanding the internal thermal state of the SCS and may provide information concerning its lithospheric structure. Therefore, we collect nearly hundreds of heat flow data from the published literature and the Guangzhou Marine Geological Survey to discuss their geothermal characteristics (e.g., He et al., 2001; Liu et al., 2002; Mi et al., 2009; Shi et al., 2003; Xu et al., 2006, 2018; Zhang & Wang, 2000 etc.). Additionally, 110 Mw/m^2 in Core 367-U1499 (18.4095°N, 115.8598°E), 100.1 Mw/m^2 in Core 368-U1501 (18.8849°N, 115.7658°E), and 94.0 Mw/m^2 in Core 368-U1505 (18.9176°N, 115.8590°E) are collected from IODP367/368 reports (Jian et al., 2018; Sun et al., 2018). A contour map of these heat flow measurements is present in Figure 10.

2.1.3. Reflection Seismic Data

Numerous seismic experiments have been carried out in the northern SCS continental margin by the China National Offshore Oil Corporation (CNOOC). The reflection profile line 1 from CNOOC, which has been processed by a standard procedure, including filtering, multiple suppressing, stacking, and time migration, will be interpreted to understand the deep crustal structure of the SCS margin. Parameters in the seismic surveys are summarized as follows: the air gun volume is larger than 4,100 in.^{3} (0.067 m^3), the shot point

interval is 50 m, the dominant frequency of the signals is 75 Hz, the vertical resolution is 8–10 m, and the streamer is 7.2 km long with 576 channels.

2.2. Modeling Approach

A series of numerical experiments are performed using a modified 2-D thermomechanical code based on the open-source matlab code from Gerya (2010), which is based on finite differences and marker-in-cell techniques. It solves momentum, continuity, and heat conservation equations for a 2-D creeping flow. We employ a visco-plastic-elastic rheology for the numerical materials. The rheological behavior is based on the minimum creep viscosity by comparing the ductile and brittle/plastic deformation field (Ranalli, 1995). Partial melting is implemented by experimentally determined wet solidus and dry liquidus curves in the pressure-temperature domain (Burg & Gerya, 2005; Gerya & Yuen, 2003). A weak stick air/water layer ($\eta = 10^{18}$ Pa·s, $\rho = 1{,}000$ kg/m^3) overlies the crust and provides a free-surface-like condition that allows the evolution of topography (Crameri et al., 2012; Schmeling et al., 2008). The interface between the water layer and the underlying crust is designed as an internal erosion/sedimentation surface, which solves the diffusion equation on the Eulerian nodes at each time step (Gerya & Yuen, 2003). A constant gross-scale erosion/sedimentation rate of 1 mm/year is used in our models. More details about the numerical method are available in Governing Equations S1 in the supporting information.

2.3. Initial and Boundary Conditions

Our numerical experiments are conducted in a 400×450 km box with a uniform rectangular grid (a resolution of 2×2 km) and randomly distributed markers (about 3 million). The mechanical boundary conditions are free slip at all boundaries, except that the lower boundary has a vertical inward velocity that changes at each time step. We initiate extension by applying a constant time-independent velocity of ±3.0 cm/year at the left and the right model side (Barckhausen et al., 2014). The stick air/water layer is 7 km thick. Our two-layer crust model consists of the upper and lower continental crust of differing rocks with a total thickness of 35 km. The upper continental crust is composed of quartzite rheology, and its strength is predicted by the Mohr-Coulomb fracture criterion and thermally activated flow law. The lower continental crust is represented by plagioclase. The strength of mantle is given by dry olivine rheology (Ranalli, 1995). As shown in Figure 2b, two brittle-ductile transitions occur within the continental crust at depths of 22 and 32 km for a nominal strain rate of 10^{-14} s^{-1}.

The three-layer-crust model has a LVCL between the upper and lower crust (Figure 2a). The other model settings are the same as the two-layer-crust model. A scaling factor f is used to produce stronger or weaker rheological strength than the base set, which is calculated from reference quartzite (Figure 2c). The LVCL deforms by ductile flow and exhibits different ductile strength by varying the scale factor f (Figure 2c). Obviously, the strength of the LVCL increases as the f increases. For example, the lowest ductile strength of the LVCL is 1.3 MPa with a scale factor of 0.1, whereas the strength at a scale factor of 1 is 3.2 MPa, which is 2.5 times stronger. The thickness and rheological strength of the LVCL are both varied to analyze their influence on the development of rifted margin. Rheological laws for all solid rocks are given in Table S1 in the supporting information.

The initial thermal structure of the continental crust is laterally uniform. Vertically, the temperature increases from 0 °C at the 0 km to 1380 °C at 82 km linearly (Blanco-Quintero et al., 2011). The gradient in the asthenosphere is 0.5 °C/km. Both sides of the model are insulated. We prescribe a small thermal heterogeneity in the lithospheric mantle to initially generate a temperature perturbation in the middle of the model (Figure 2a). Increasing temperature reduces the effective viscosity of the rocks, and lower viscosity further attracts the deformation (Burg & Gerya, 2005; Hartz & Podladchikov, 2008).

3. Model Results

3.1. Influence of the LVCL

For the two-layer-crust model, intense strain localization occurs around the temperature perturbation and propagates into the crust in the early extension stage, forming two conjugated lithosphere-scale shear zones (Figure 3a). During progressive strain localization in the lithospheric mantle, the strength of the mantle decreases. As a result, the mantle necking starts and becomes the dominant mechanism to accommodate lithospheric deformation. Simultaneously, the mantle necking can result in obvious lithospheric thinning
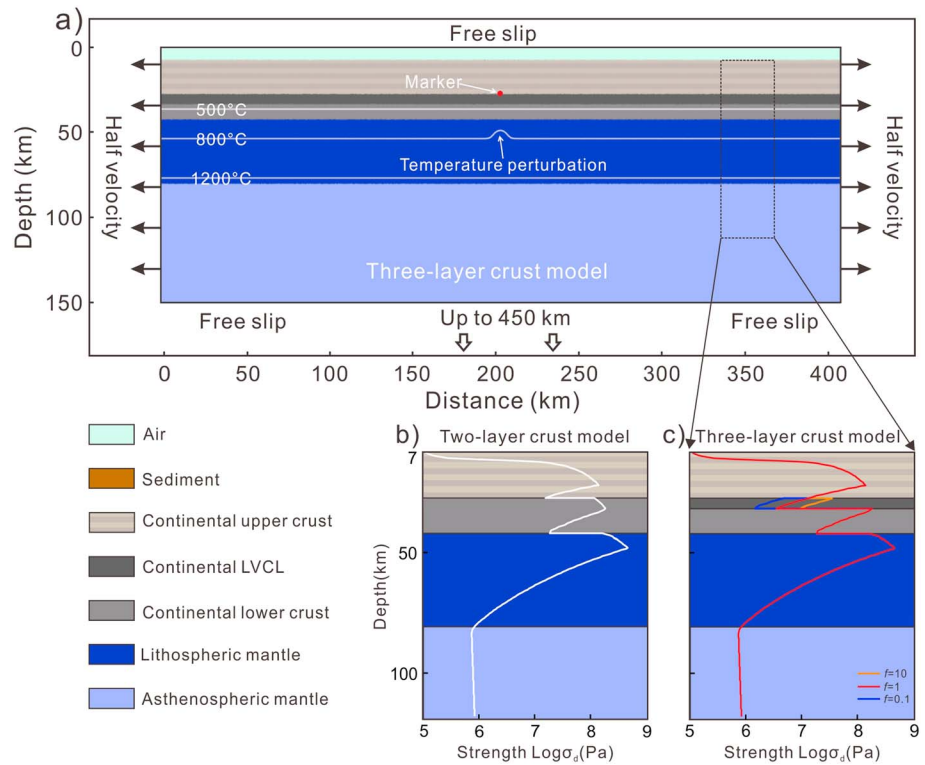
Figure 2. Initial setups of the three-layer-crust model with an enlarged 400×150-km domain of the original 400×450-km model and yield strength profiles. A LVCL is embedded in the continental crust, and its rheology and thickness vary in different models. Horizontal velocity of 3 cm/year is applied on both sides of the model (arrows). White lines are isotherms measured in Celsius. The colors represent the different rock types. For more initial and boundary conditions, please see the text. The marker is used to trace the evolution path. A rectangular region in Figure 2a is used to calculate the strength profile. Strength profile for the two-layer-crust model is a reference case (Figure 2b). As shown in Figure 2c, the LVCL deforms by ductile flow, and the rheological strength of the LVCL increases with increasing *f*. LVCL = low-viscosity crustal layer.
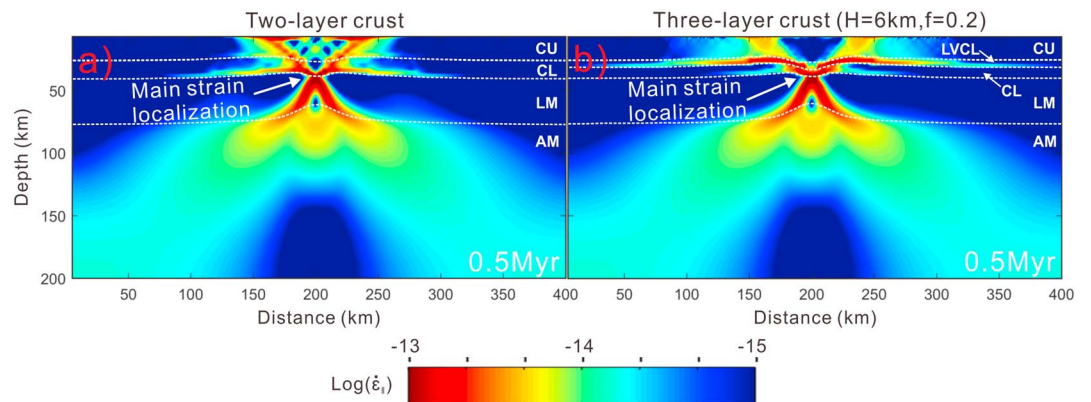

Figure 3. Second invariant of the strain rate for the two-layer-crust model (a) and three-layer-crust model (b) in 0.5 Myr during lithospheric extension. Major conjugate shear bands cutting across the crust and lithospheric mantle form in the two-layer-crust model. For the three-layer-crust model, however, strain mainly localizes in the low-viscosity crustal layer and underlying lithospheric mantle and there weakly develops strain localization in the upper crust. CU: continental upper crust; CL: continental lower crust; LM: lithospheric mantle; AM: asthenospheric mantle.
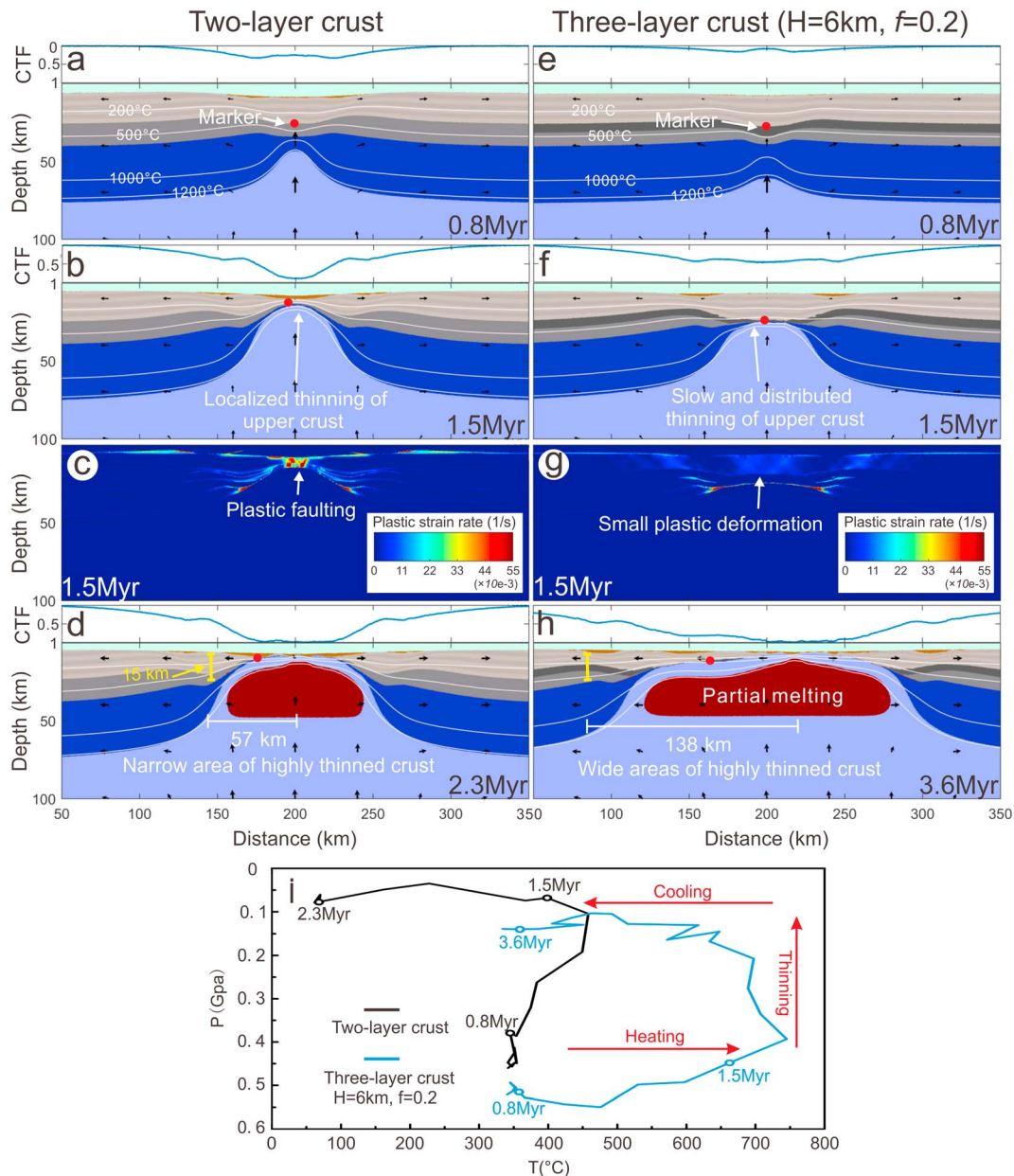
Figure 4. Evolution of the two-layer-model (a–d) and three-layer-crust ($H = 6$ km and $f = 0.2$; e–h) model. The red solid circles indicate the position of representative markers for which the P-T-t paths are shown in Figure 4i. CTF = crust thinning factor. The thinning evolution of the crust is shown with CTF, which is defined by $(H_0 − H_1)/H_0$, where H_0 is the initial thickness of the crust and H_1 is the crustal thickness at a given time. When the CTF reaches 1, the upper crust ruptures. Rock types and temperature isotherms are the same as in Figure 2. Arrows are velocity vectors of Vx and Vy.

and hot asthenospheric upwelling, so that the 1200 °C isotherm rises up to the lower crust level (Figure 4a). The P-T-t paths of the representative material marker show a rapid decrease in the pressure before 1.5 Myr (Figure 4i). These conditions indicate that the crust undergoes continuous decompression and exhumation as the hot asthenosphere upwells. Rift basin forms on the surface with synrift sediment infill.

As extension proceeds, the crust starts to rupture and exhibits a crustal thinning factor of 1 (Figure 4d). Meanwhile, a narrow transitional region (~57 km wide), where the continental crust thins abruptly, are eventually developed. The material marker has been carried to the near surface and involved into the crustal fragment. It cools with time due to decreasing heat supply and heat loss by conduction (Figure 4i). Asthenospheric mantle partially melts and exposes to the surface (Figure 4d). These modeling results agree with geological field investigations and previous simulations (Duretz et al., 2016; Liao & Gerya, 2014).

By contrast, there are significant differences when a LVCL is embedded in the middle of the crust. Strain mainly localizes in the LVCL and underlying lithospheric mantle. The upper crust, however, only has weakly developed strain accumulation (Figure 3b). The possible explanation is that the lateral ductile flow in the LVCL decouples the upper crust from underlying layers mechanically and accommodates the deformation generated by extension. This leads to a situation that the deformation localization in the upper crust is delayed. As a result, the upper crust thins slowly in the early extension stage. For example, the upper crust is less stretched and remains relatively little thinning at 1.5 Myr (Figure 4f), denoting a phase of slow and distributed continental rifting. At the early stage, the ductile crustal flow also acts as an effective layer to compensate the gravity isostasy, allowing for very low topographic gradients. As a result, there lack a large sedimentary basin on the surface.

Since the continental lithosphere mantle and lower crust have been replaced by the upwelling asthenosphere preferentially, the upper crust touches the hot upwelling asthenosphere (Figure 4f) and gets heated due to conductive heat transfer. As shown in Figure 4i, the temperature for the material marker continues to increase till ~1.6 Myr and reaches the peak value of ~750 °C. The heat can be conducted to the surface from depth, and thereby, high surface heat flow can be estimated in nature (Lenardic et al., 2005; Turcotte & Schubert, 2014). During further extension, continuous heating weakens the upper crust (Figure 4g). The deformation mechanism in the upper crust is gradually governed by a thermally activated viscous power law, ductile flow. As a result, the crustal deformation is not localized but distributed over a broad area (Figures 4f and 4g). Such deformation results in a longer duration from crustal extension to broken and thus increases the width of highly thinned continental crust.

After diverging for ~3.6 Myr, the extension becomes more effective at crustal thinning and eventually ends up by the continental breakup. The representative material marker begins to move upward and undergoes decompression (Figure 4i). As shown in Figure 4h, the upper crust extends over a broad area and eventually breaks apart, forming a hyperextended margin. The transition from a 15-km-thick upper crust to a zone of exhumed asthenospheric mantle occurs over a distance of ~138 km. This transition is much more gradual compared to the two-layer crust model. The final breakup is not initiated in the middle of the model but on the left side. It leads to the development of asymmetric margin and leftward migration of the rifting center (Figure 4h). Continental crust cools progressively after reaching the near surface, similar to the results obtained from the two-layer-crust model (Figure 4i). During the 3.6 Myr of extension, the asthenospheric materials rise up with decompression and generate significant melts. The melts probably will first underplate the continental crust, then intrude it, and finally extrude the crust. As soon as the crust breaks, this magmatic product will generate a protooceanic crust, in accord with the results of IODP367/368 drilling that found no exhumed or serpentinized mantle at the surface (Sun et al., 2018).

3.2. Variable LVCL Strength

The effective viscosity of the ductile crustal layer is scaled linearly by a factor f, which varies from 0.01 to 100. The f represents different rheological strength that is stronger or weaker than that of the reference set. With the same thickness of 6 km, results obtained from various f are presented in Figure 5, such as f of 0.01, 0.2, and 100.

When the scale factor is 0.01, the model experiences a slowest crustal thinning (Figure 5b). For example, the thinnest crust appears at 200 km and only has a thinning factor of ~0.41 at 1.5 Myr. Since the thinning of the crust is largely reduced, the continental breakup occurs relatively late (~4.1 Myr; Figure 5b′). There also develops a wide hyperextended margin, which exceeds 180 km (with a thickness of <15 km). By contrast, the models with f of 0.2 and 100 have stronger strength and exhibit a greater degree crustal thinning. At 1.5 Myr, about 47% and 85% of the crust are removed in these two models, respectively (Figures 5c and 5d). In particular, the model with f of 100 even shows characteristics of localized deformation. As a result, the models with f of 0.2 and 100 are broken apart in a shorter period (approximately 3.6 and 2.6 Myr). Meanwhile, the width of highly thinned crust is significantly reduced. It spans ~138 km for the model with a scale factor of 0.2 and ~94 km for the model with 100 (Figures 5c′ and 5d′). Therefore, our results show that the duration of crustal extension and width of highly thinned margin (thickness of ≤15 km) is inversely proportional to the strength of the LVCL when the other parameters are constant. A weaker LVCL results in a longer crustal extension stage and wider hyperextended margin.
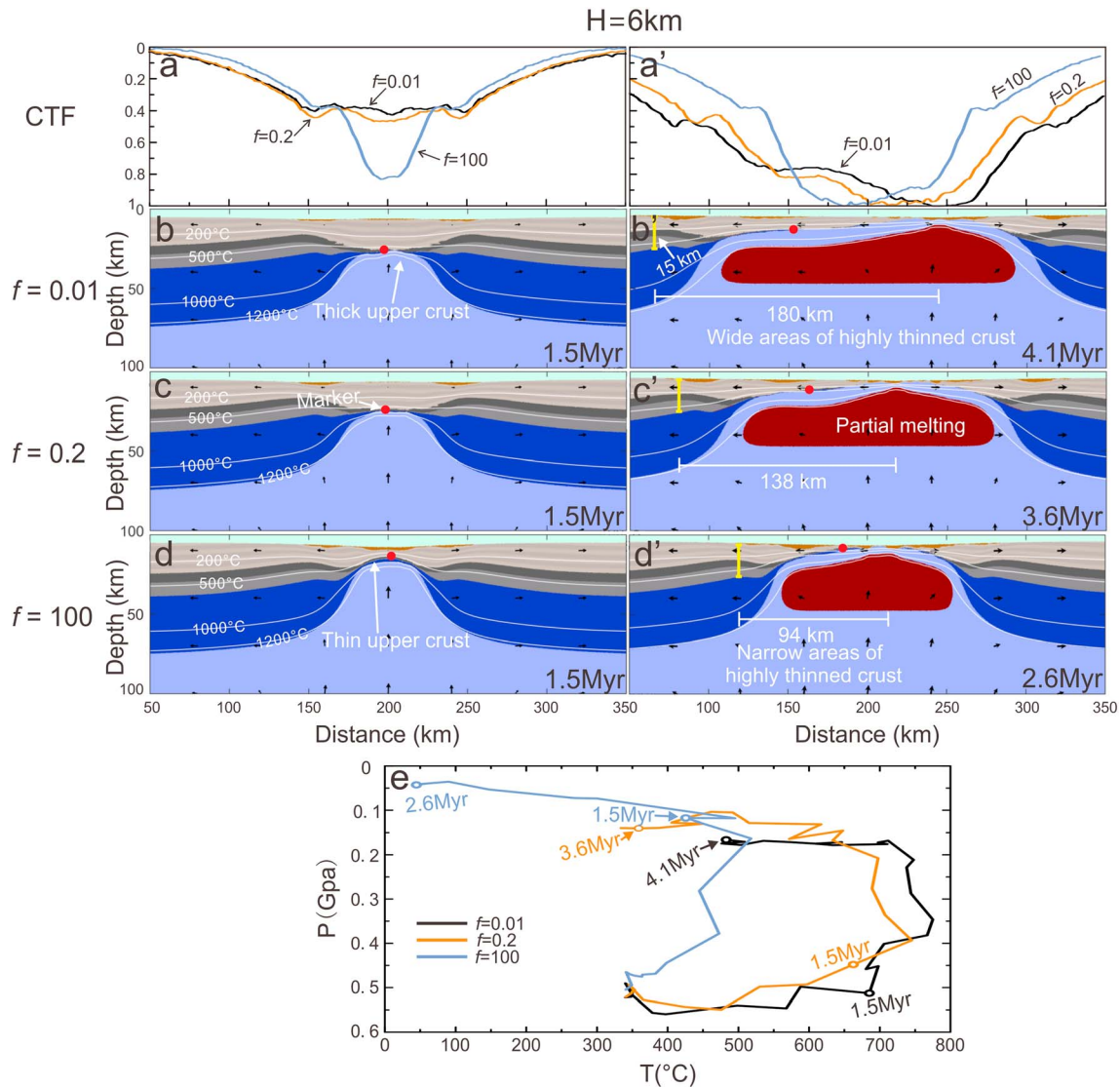
Figure 5. Evolution of the three-layer-crust model with f of 0.01 (b, b'), 0.2 (c, c'), and 100 (d, d'). The red solid circles indicate the position of representative markers for which the P-T-t paths are shown in Figure 5e. It is noteworthy that a smaller scale factor could results in a higher temperature during extension. The thickness of low-viscosity crustal layer for each model is constant ($H = 6$ km). The evolution of upper crust thinning is also shown with CTF (a, a'). Rock types and temperature isotherms are the same as in Figure 2. Arrows are velocity vectors of Vx and Vy. CTF = crust thinning factor.

As revealed by P-T paths in Figure 5e, the temperature of material marker raises from 350 to ~600–800 °C, depending on the value of the scale factor. Similar to the development of hyperextended crust, a smaller scale factor also results in a higher temperature on the near surface. For example, a scale factor of 0.01 promotes the temperature up to ~800 °C, while the maximum temperature is only ~ 500 °C if the f is 100.

3.3. Variable LVCL Thickness

A series of numerical models with different LVCL thickness is further investigated. The initial scale factor for the models is 0.2, and the other parameters are the same as previous models. When the LVCL is 1 km thick, the model produces intense crustal thinning. A large portion of the crust thickness (~85% of total) is reduced at 1.5 Myr (Figure 6b). Less than 1 million years later, the continent starts to break apart and develops a narrow hyperextended margin, which only extends approximately 81 km from the spreading center. The thinning of the crust is greatly reduced when the thickness increases to 4 and 6 km. At 1.5 Myr, about 72% and 47% of the total crust are removed from the models with thickness of 4 and 6 km,
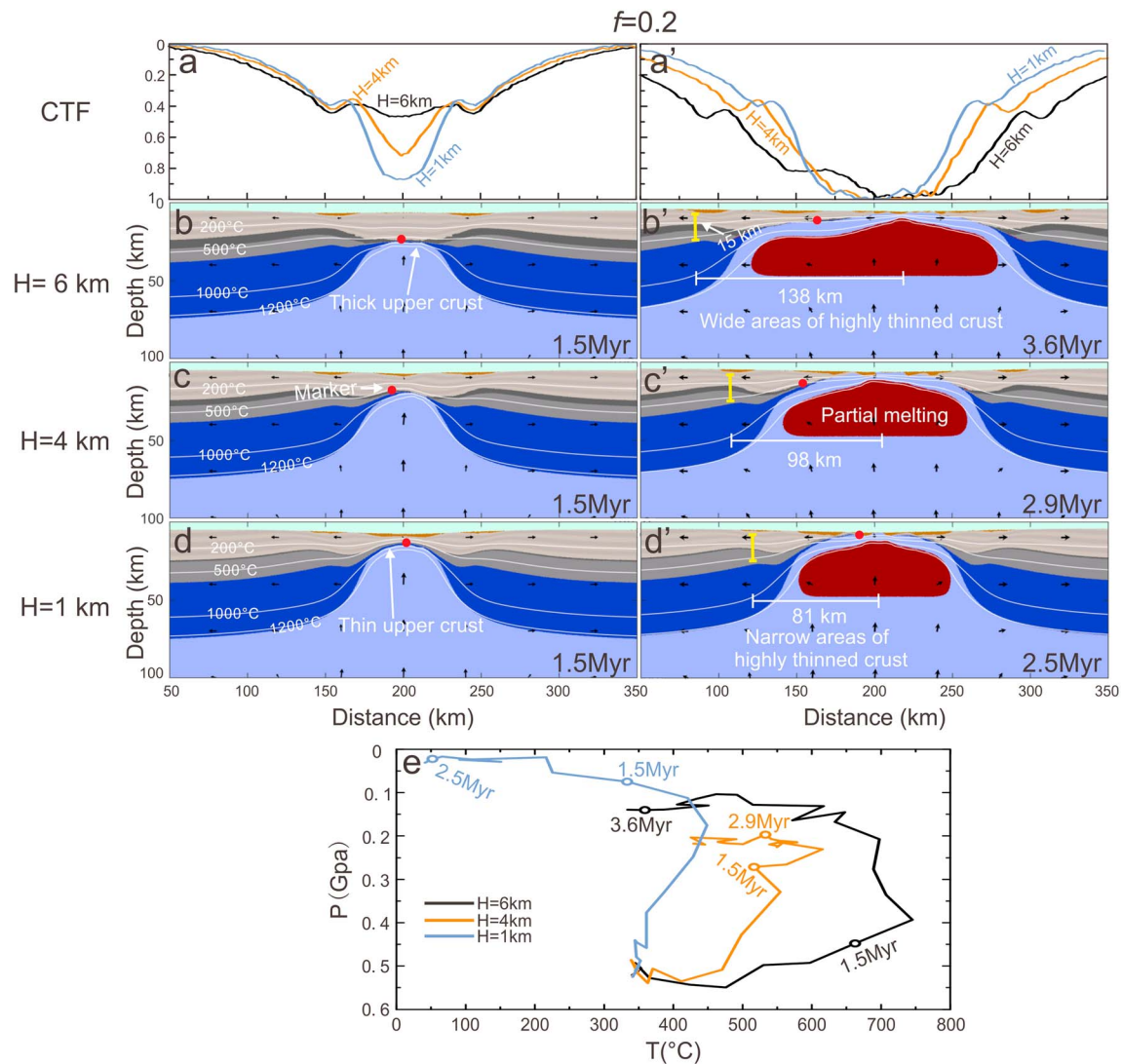
Figure 6. Evolution of the three-layer-crust model with H of 6 (b, b′), 4 (c, c′), and 1 km (d, d′). The red solid circles indicate the position of representative markers for which the P-T-t paths are shown in Figure 6e. A thinner LVCL has a lower temperature at a certain time. The scale factor of the LVCL for each model is constant (0.2). The evolution of upper crust thinning is shown with CTF (a, a′). Rock types and temperature isotherms are the same as in Figure 2. Arrows are velocity vectors of V_x and V_y. LVCL = low-viscosity crustal layer; CTF = crust thinning factor.

respectively (Figures 6c and 6d). As a result, the final breakup of these two models is delayed accordingly. During continued extension, both of the models exhibit an increase in the width of highly thinned crust. The widths are approximately 98 and 138 km (Figures 6c′ and 6d′). Therefore, our results manifest that the duration of crustal extension and width of highly thinned crust increase with the thickness of the LVCL. That is, a thicker LVCL prolongs the crustal extension time and promotes the formation of a wider highly thinned crust.

Our results also indicate that the maximum temperature increases with the thickness of the LVCL due to prolonged heating. As shown in Figure 6e, the model with a thickness of 6 km experiences the longest time crustal thinning (~3.6 Myr) and, as a result, the crust was heated to be the hottest case (~750 °C).

3.4. Variable Extension Velocity

In this section, numerical experiments with different half-extensional velocities (e.g., 1, 1.5, 2, and 3 cm/year) are conducted to test their effects on the development of rifted margin. The thickness and scale factor of the LVCL are 6 km and 0.2 for each model. Obviously, the extension in the models by higher velocities
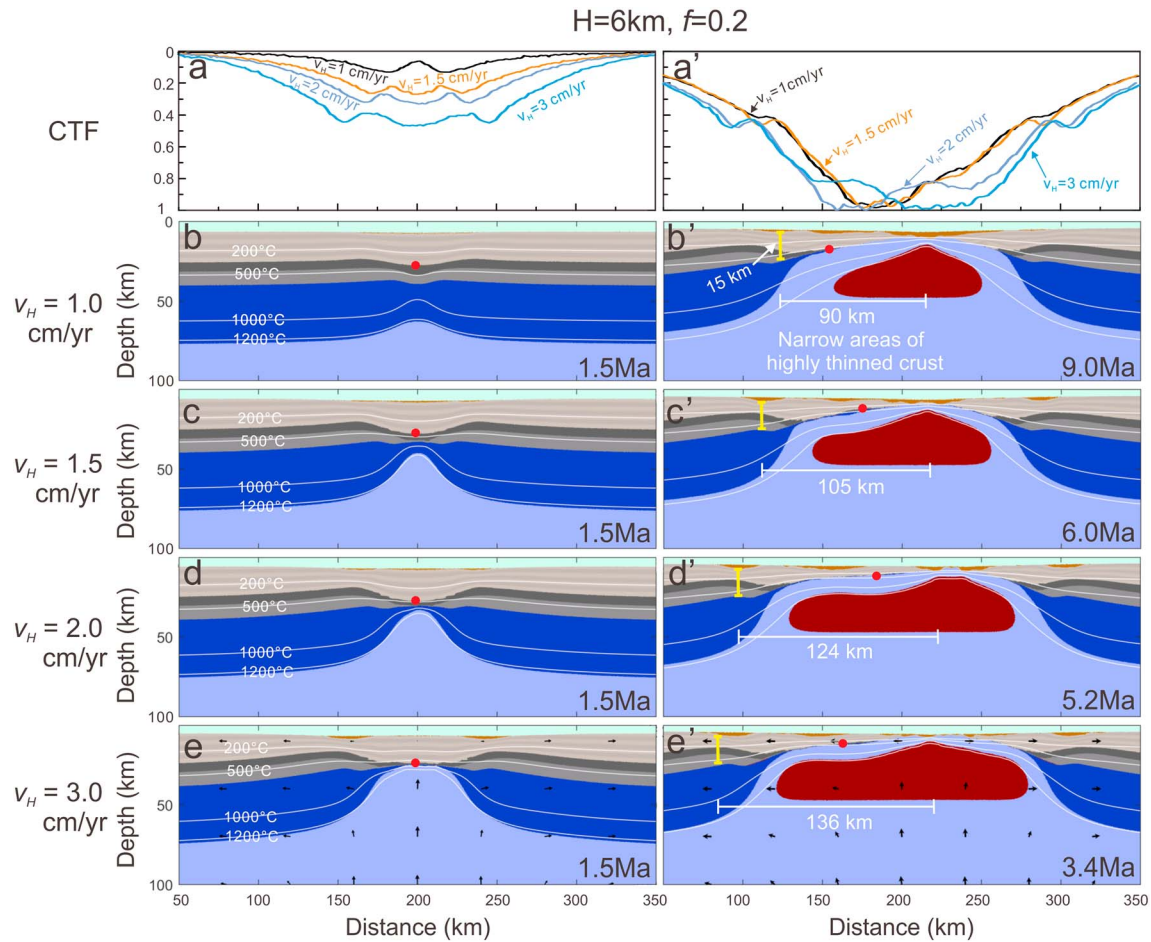
Figure 7. Evolution of the three-layer-crust model with half extension velocity of 1 (b, b′), 1.5 (c, c′), 2 (d, d′), and 3 cm/year (e, e′). The thickness and scale factor of the low-viscosity crustal layer are 6 km and 0.2. The evolution of upper crust thinning is shown with CTF (a, a′). Denotations are the same as those in Figure 2. Arrows are velocity vectors of Vx and Vy. CTF = crust thinning factor.

evolves more quickly. For instance, in 1.5 Myr, about 13%, 26%, 33%, and 47% of the total crust thickness are reduced for half-extensional velocity of 1, 1.5, 2, and 3 cm/year (Figures 7b–7e), respectively. More differences among these models appear when the continent breaks, such as the width of highly thinned crust. It spans ~90 km for the model with half-extensional velocity of 1 cm/year (Figure 7a′). In comparison, for the model with a velocity of 6 cm/year, the highly thinned crust extends ~138 km (Figure 7e′). That is, the higher velocity could cause a wider highly thinned crust.

4. Geological Implications for the Northern SCS Continental Margin

The northern SCS locates at the southern edge of the South China block and is a passive continental margin (Figure 1a). The SCS margin includes a series of extensional basins (e.g., the Pearl River Mouth Basin and the Tai Xi Nan Basin) and evolved from rifting of the South China block since post-Cretaceous (e.g., Ding et al., 2018; Franke et al., 2014; Li, Sun, & Yang, 2018; Lin et al., 2019; Morley, 2016; Tapponnier et al., 1990). As such, studies on the northern SCS margin can help us understand the consequences of lithospheric extension with a weak middle crustal layer.

4.1. Crustal and Geothermal Characteristics of the Northern SCS Margin

To obtain the crustal thickness in the SCS area, we first calculate the geometry of the Moho discontinuity using gravity data. The data source and processing method have been briefly introduced in the method section. Figure 8 is the map of Moho depth of the northern SCS margin derived from 3-D gravity modeling. We use
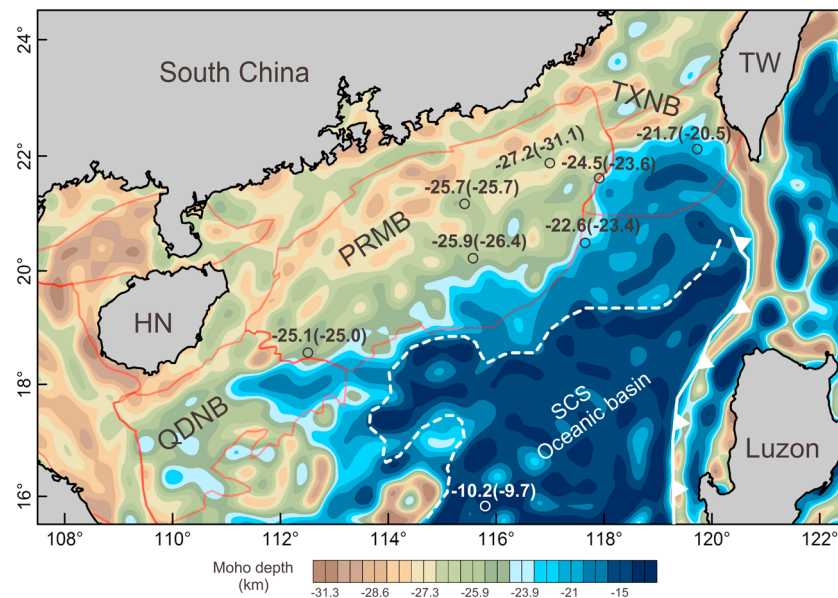
Figure 8. Moho depth map of the northern SCS margin obtained from the 3-D gravity inversion. Locations of seismic control points are shown as black circles. Gravimetric and seismic Moho depths of these control points are listed in and out of the brackets, respectively. SCSB = South China Sea Basin; PRMB = Pearl River Mouth Basin; TXNB = Tai Xi Nan Basin; TW = Taiwan; HN = Hainan.

the depths that derived from the deep seismic profiles to constrain the validity of the gravimetric solutions. At the constraint points, the average misfit between the inversion results and the seismic depths is less than 1 km (Figure 8). For example, the Moho depths in the Pearl River Mouth Basin are computed to be 25.1, 25.9, 22.6, and 24.5 km, which are rather close to the depth (25, 26.4, 23.4, and 23.6 km) revealed by the deep seismic profiles (Fan et al., 2019; Qiu et al., 2001; Ruan et al., 2011; Wang et al., 2006; Wei et al., 2011; Yan et al., 2001; Yeh et al., 2010). The depth 21.7 km in the Tai Xi Nan Bain is also verified by the seismic depth (20.5 km; McIntosh et al., 2005). The minor misfit implies a good quality of inversion result for a range of Moho depths between 10 km (deep ocean basin) and 31 km (continental margin).

We then estimate the crustal thickness of the SCS by subtracting the bathymetry and sedimentary thickness from the Moho depth. As shown in Figure 9c, the SCS basin reveals an average crust thickness of ~6 km, except that the ridges and seamounts have a thicker crust of 10–20 km. These results are consistent with previous studies (Lü et al., 2011; Qiu & Chen, 2011). The thickness of the continental crust is highly variable. In the northeastern margin, continental crustal thickness shows a remarkable gradual increase from the ocean-continent boundary (OCB) to the continental slope. A very thin continental crust of ≤15 km extends over distances of 100–250 km from the OCB. In contrast, the northwestern margin has another scenario. The transition from OCB to a thickness of 15 km appears rather narrow. The thickness keeps increasing toward the continental shelf to values as large as ~28 km. As a result, the northwestern margin only has a narrow ultrathinning continental crust. In summary, our results illustrate a significant contrast along strike of the northern SCS margin regarding the width of ultrathinning crust. The ultrathinning continental crust is wide in the northeast but narrow in the southwest. Similar phenomena were also observed by other researchers, such as Bai et al., 2019, Yeh and Hsu (2004), Tsai et al. (2004), Qin et al. (2011), and Pichot et al. (2014).

In the northern continental margin, the high heat flow region in the northeast also spans wider than that in the northwest. See Figure 10, nearly hundreds of heat flow data were compiled in a contour map. The heat flow value increases from the shelf toward the oceanic basin, ranging from 35 to 120 mW/m^2. The SCS oceanic basin is a high heat flow zone with an average value of 93 mW/m^2. Although the heat flow in the SCS margin is significantly lower than that in the ocean basin, there also exits a relatively high heat flow zone trending NE, lying on the lower slope area of the northern SCS margin (Shi et al., 2003). The high heat flow zone in the northeastern SCS margin extends ~200 km in the N-S direction, which is clearly wider than the zone in the northwest.
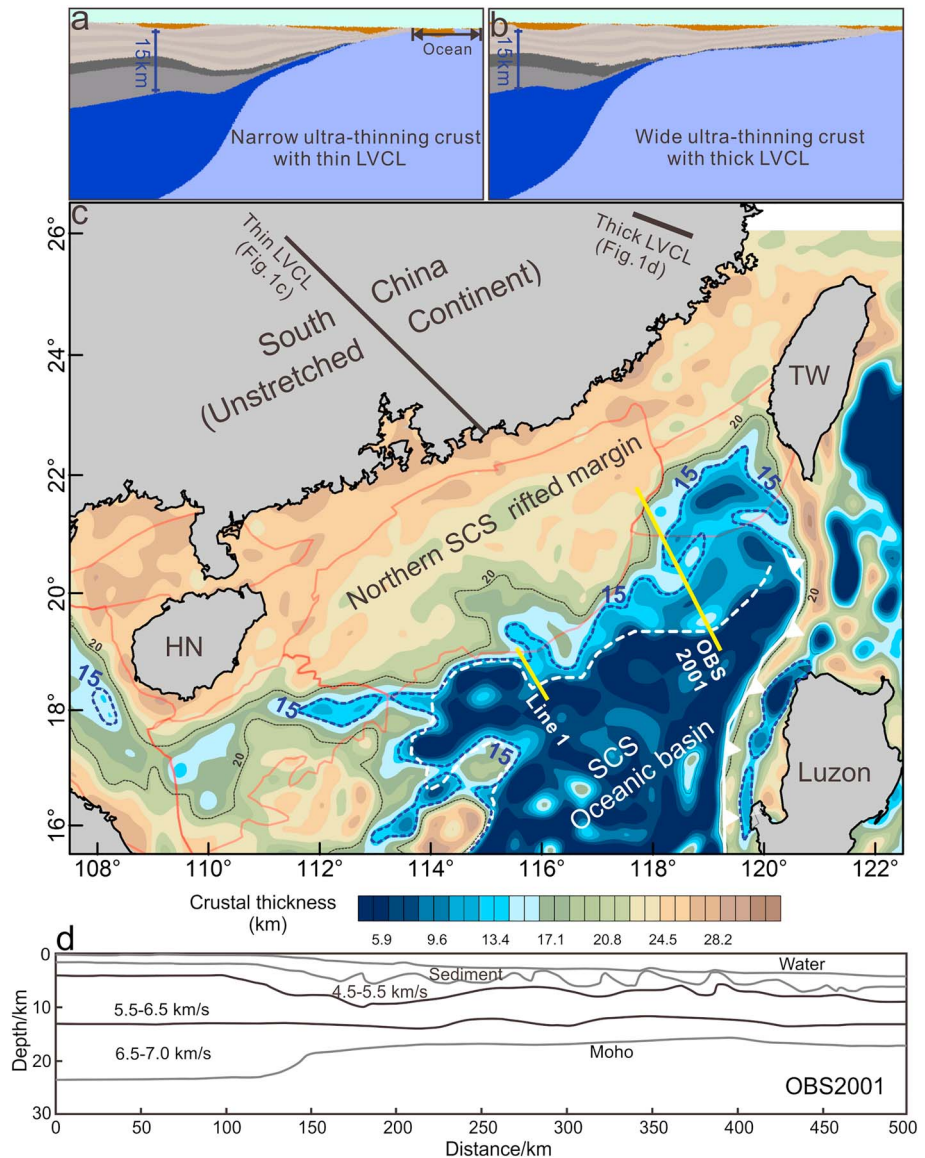
Figure 9. Compare model results with widths of highly thinned crust in the northern SCS margin. (a, b) Model results showing the widths of ultrathinning crust with different low-viscosity crustal layer thickness. (c) Crustal thickness map of the northern SCS margin. (d) *P* wave velocity model with layer boundaries of OBS2001 (Wang et al., 2006). In the Figure 10c, a very thin continental crust of ≤15 km extends over distances of 100–250 km in the northeast (black double arrow). In contrast, the thickness of ≤15 km appears rather narrow in the northwest. Yellow lines represent the location of profile line 1, and the detailed crustal structures are shown in Figure 11. Red and white lines outline the boundary of continental and oceanic basins. SCS = South China Sea; TW = Taiwan; HN = Hainan.

4.1.1. Comparison of the Model Results With the Along-Strike Variation of Highly Thinned Crust Width in the Northern SCS Margin

By comparing the two profiles in the South China continent interior (Figure 1), it is evident that there exist obvious differences in the initial LVCL thickness. The LVCL in the east is clearly thicker than that in the west (Figures 1 and 9c). Meanwhile, in order to further constrain the thickness of the middle crustal layer in the eastern margin, we select a refraction seismic profile OBS2001 to survey the deep crustal structure (Figure 9d). The profile OBS2001 crosses the Taixinan basin and finally extends southeastward into the east subbasin (Wang et al., 2006). The crust thins from about 25–28 km beneath the continental shelf to 13–15 km beneath the ocean-continent transition zone. The ultrathinning part of the continental crust (≤15 km) extends about several hundred kilometers along the profile OBS2001, agreeing with our gravimetric
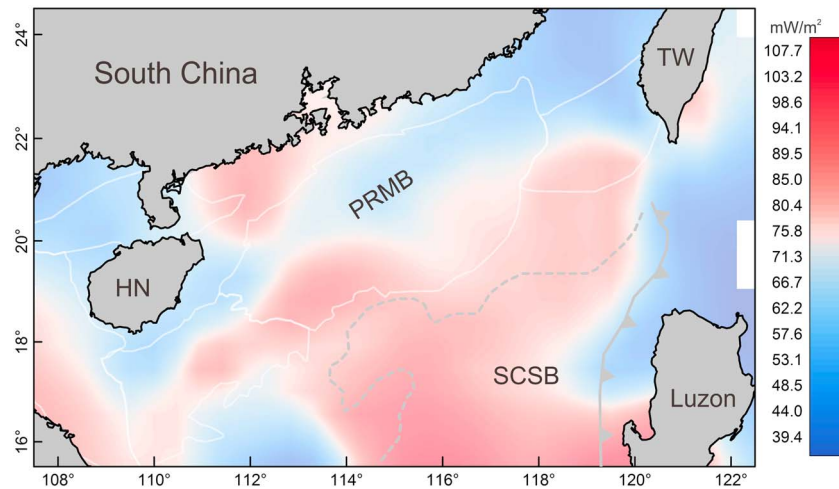
Figure 10. Spatial distribution of heat flow measurements in the northern SCS (compiled after He et al., 2001; Shi et al., 2003, 2017; Yuan et al., 2009). The N-S direction high heat flow zone in the northeastern SCS margin extends wider than the zone in the northwest. White lines outline the boundary of continental basins. SCSB = South China Sea Basin; PRMB = Pearl River Mouth Basin; TW = Taiwan; HN = Hainan.

solutions. In addition, a middle crustal layer can be observed lying within the crust with *P* wave velocity of 5.5–6.5 cm/year. It has an average thickness of ~6 km, which is clearly thicker than that in the west (~3 km). That is, the northeastern SCS margin may forms by stretching the South China continent with a thick LVCL, whereas the northwest margin evolves from the continent with a relatively thin LVCL. The initial LVCL thickness also has a good correspondence with the width of highly thinned crust (Figure 9c). The northeastern margin shows characteristics of thick LVCL and wide ultrathinning crust. In comparison, the northwestern margin is characterized by thin LVCL and narrow ultra-thinning crust. These phenomena are consistent with our numerical results in which a thicker LVCL can induce a wider hyperthinning crust (Figure 9). Thereby, as one possibility, the initial LVCL thickness plays a great role in controlling the crustal thickness in the northern SCS margin. A thicker LVCL exists on the northeastern SCS margin and thus induces a wider ultrathinning crust. A thinner LVCL in the northwestern SCS margin causes a narrower ultrathinning crust. In summary, our studies suggest that variation in the weak ductile layer thickness may be a cause for the differential stretching characteristics in the northern SCS margin.

It is worth emphasizing that other hypotheses also have been proposed to explain this along-strike variation. For example, Wang et al. (2006) attributed the phenomena to the eastward subduction of the Eurasian Plate along the Manila Trench near the northeast. However, the subduction started at early Middle Miocene, which is much later than the termination time of the SCS continental breakup (~39 to ~21 Ma; Huang et al., 2012; Sibuet & Hsu, 1997; Sun et al., 2011). Thereby, the subduction of the Eurasian plate cannot affect the rift structure of the SCS margin. Another possibility is that the upwelling mantle may attenuate the continental crust in the east, causing the development of a wide zone of highly thinned crust (Mao et al., 1999). If so, the lower crust would get heated and flows laterally during extension, thus generating a variable lower crust thickness. However, according to the evidence from deep seismic profiles across the ultra-thinning crust zone (e.g., OBS2001), it seems that there is no obvious variation in the lower crust thickness (Qiu & Chen, 2011). Yao (1998) viewed the highly thinned crust as a result of erosion in the Cenozoic, which remove large amounts of rocks from the upper crust. In this case, the removal of rocks from upper crust will be isostatically compensated by lower crust and mantle rebound, which in turn cause tectonic or isostatic uplift in the region. However, the northeastern SCS margin is a topographically lower area, and this contradicts what was expected above. Thereby, our models offer one possible mechanism by which differential widths of ultrathinning crust develop in the northern SCS margin.

Our models also predict a high extension velocity to reproduce the observed width of the SCS margin. This prediction is consistent with the results of 3-D thermomechanical models in which rift propagation occurs during extension (Le Pourhiet et al., 2018). Propagation of continental breakup changes the dynamics of continental rifting and, as a result, the continental extension rate on the west margin is likely to be larger than during the

continental rifting of the east margin (e.g., Le Pourhiet, 2018; Vink, 1982). Their extension rate in the west margin is equal to the spreading rate that also agrees with our modeling results. Previous studies have investigated how the lower crust rheology controls the rate of continental break-up propagation and the width of the passive margin (e.g., Burov & Watts, 2006; Liao & Gerya, 2015; Pérez-Gussinyé et al., 2003). Yet the influences of weak middle crustal layer on the propagation rate and margin width are still uninvestigated. In this paper, the effects of LVCL on the width of rifted margin are qualitatively evaluated by 2-D models. Despite simplifications, the 2-D models can be considered representative for the end-member of continental extension with LVCL embedded. Compatibility of the model with the geologically realistic results has been demonstrated above. Our models offer one possible mechanism by which wide ultra-thinning crust might develop in the northeastern SCS margin. The other factors, such as the rift propagation and ridge jump, also play a great role in the width of the SCS margin, but a combination of these factors is beyond the scope of this paper. In the future work, we hope to consider these factors and expect a result much closer to the observations.

4.1.2. Possible Reasons for the Geothermal Characteristics of the Northern SCS Margin

In the northern SCS margin, an NE-SW trending high heat flow zone exists on the lower slope, and its north-south extent in the east is larger than that in the west (Figure 10). Previous studies suggested that the strong differential crust thinning is a viable mechanism explaining the situations (Huismans et al., 2001). Shi et al. (2017) pointed that the high heat flow in the northern SCS margin is not only the result of intense crustal thinning but also caused by the upwelling of hot asthenosphere during continental breakup. In addition, Lei (2013) further revealed that the thinner crust and longer mantle upwelling contributed more heat flow. By calculating the temperature and thermal structure of the SCS lithosphere, many studies argued that the upwelling of hot asthenosphere might produce the vast majority of heat flow (e.g., Zhang & Shi, 2004). Synrift sediments in the deep water also preclude the presence of high thermal anomaly during breakup (Clift & Lin, 2001). These results showed similarities to our numerical models in which the hyperextended continental crust is heated by hot upwelling asthenosphere and thus characterized by high surface heat flow over a wide area. Integrating our numerical results with observations, we emphasize the strong control of LVCL on the geothermal characteristics of the northern SCS margin. Our numerical results also demonstrated that the value of heat flow increases as the initial thickness of the LVCL increases, comparing well with the characteristics in the northeastern SCS margin where wide high heat flow zone and thick LVCL are observed.

5. Discussion

5.1. Comparison to the Geothermal Characteristics of Rifting Phase in the Pyrenean

Another example comes from the rifting phase in the Pyrenean that is a result of rotation of Iberia relative to Europe in ~83–125 Ma (e.g., Lagabrielle & Bodinier, 2008; Masini et al., 2014; Sibuet et al., 2004). In the Pyrenean, the heat recorded in the synrift sediments reflects thermal conditions inherited from former rifting phase, thus providing an opportunity to study the thermal imprint of crustal thinning (e.g., Golberg & Leyreloup, 1990; Vauchez et al., 2013). In the synrift sediments, a lateral thermal variation has been distinguished by previous studies along the north Pyrenean. The western flank of the north Pyrenean is relative cold and shows low-grade high-temperature/low-pressure metamorphism with Raman temperatures ≤350 °C, whereas the eastern flank is hot and exhibits high-grade high-temperature/low-pressure metamorphism with Raman temperatures ≥600 °C (Clerc et al., 2015; Ducoux, 2017; Golberg & Leyreloup, 1990). Results from 1-D thermokinematic modeling suggested that the abnormally high temperatures possibly record a heating phase during the extreme extension (Vacherat et al., 2014). Similar effects are also obtained by our 2-D thermomechanism modeling in which the continental lithospheric mantle and lower crust have been removed prior to the upper crust in the extension, making the upper crust in direct contact with the hot upwelling asthenosphere. The heat is probably conducted to the surface from margin interior, thus making the hyperextended margin characterized by high temperature over a wide range.

Meanwhile, our models showed that the hot asthenosphere weakens the brittle portions of the upper crust, and thus, the deformation mechanism in the upper crust is gradually governed by a thermally activated viscous power law. In this situation, the crustal deformation is not localized but distributed over a broad region. This kind of deformation results in a longer duration from crustal extension to broken, thus increasing the width of highly thinned continental crust. In agreement with our modeling results, the northern Pyrenean also shows characteristics of wide areas of ultrathinning crust (Jammes et al., 2009). Nevertheless, differential stretching characteristics develop in the eastern and western flanks of the northern Pyrenean. The east
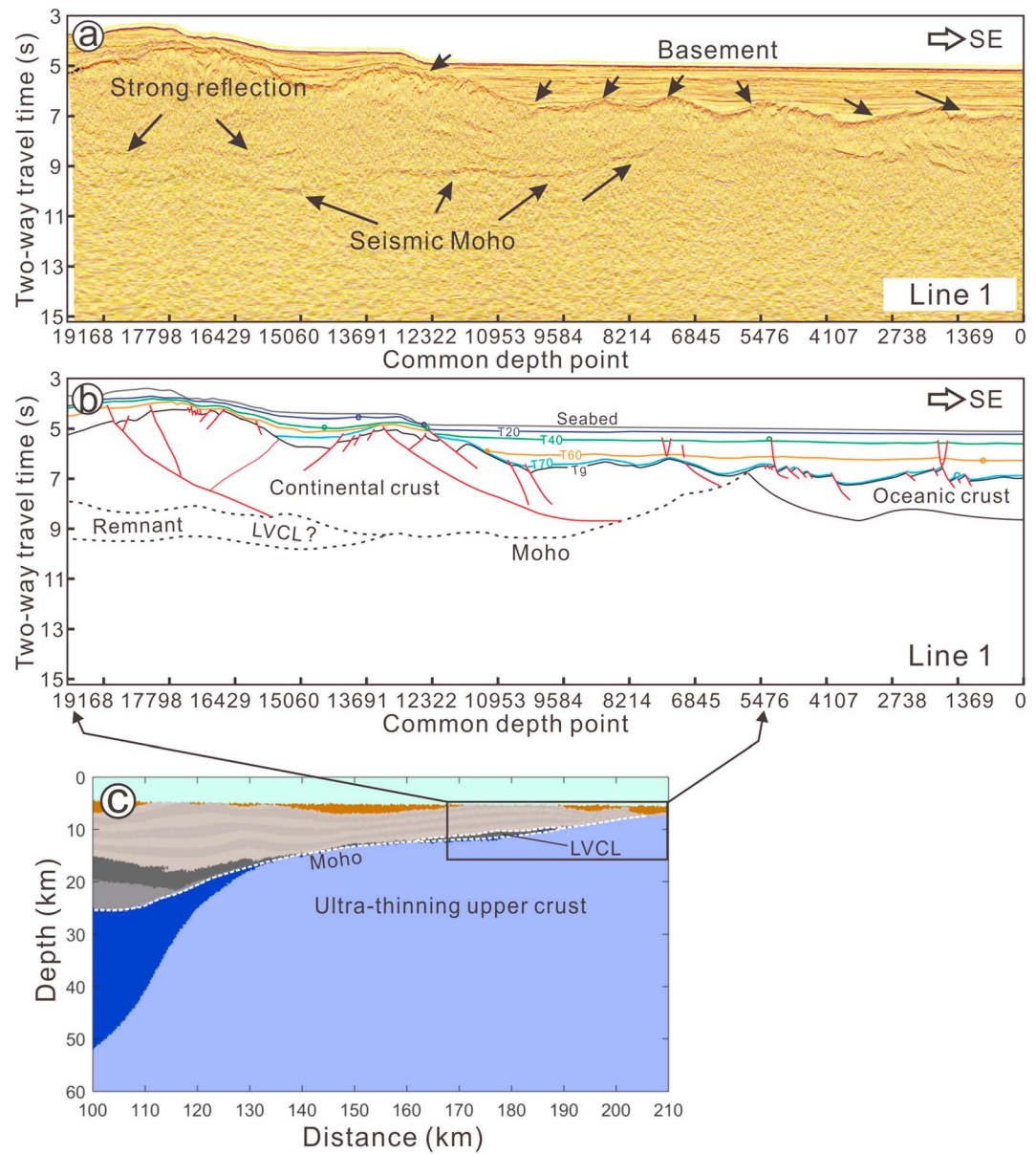
Figure 11. Seismic reflection profile line 1 without interpretation (a) and with interpretation (b). (c)Model result showing the deformation of continental margin. Ultrathinning upper crust and ductile crustal remnant can be recognized in the profile and modeling. Part of the sedimentary unconformity according to Sun et al. (2018) and Larsen et al. (2018). For location please see Figure 9.

developed extreme thin continental crust and was under a ductile regime. In comparison, the continental crust in the west is less severely thinned and dominated by brittle behavior (Jammes et al., 2009; Masini et al., 2014). Our studies further suggest that variation in the weak ductile layer thickness and/or strength may be a cause for the differential stretching and thermal characteristics in the northern Pyrenean. A weak and/or thick LVCL might exist in the east pre-Pyrenean paleo-margin and flow laterally. The lateral ductile flow accommodates the deformation generated by extension, and, as a result, hotter and wider hyperextended crust develops. For instance, the continental crust in the model with a LVCL thickness of 6 km is heated to ~750 °C and extremely stretched. Comparison with the hypotheses proposed by other authors (e.g., Fabriès et al., 1998; Golberg & Leyreloup, 1990; Jammes et al., 2009), our model well explains the regional high temperature in the eastern flank of the north Pyrenean. In addition, the model also correlates the intensity of crustal thinning to the crustal rheological behavior during extension.

5.2. Implication for the Deep Crustal Structures

Results from the three-layer-crust model show that the middle crust, lower crust, and lithospheric mantle are totally removed in the distal margin, leaving a wide region of thin upper crust in direct contact with the asthenosphere. As a result, Moho boundaries are observed beneath the ultrathinning upper crust (Figure 11c). The Moho extends landward across the distal margin and finally joins the Moho beneath the proximal margin. Meanwhile, several remnant LVCLs overlie the Moho and exhibit variable sizes. As a consequence of ductile flow in the middle crust, the surface is characterized by high topographic gradients with an abrupt change in topographic elevation in the final architecture. Sediments filled the surface topographic low.

In order to further compare these crustal structures with the natural observations, we select a reflection profile line 1 crossing the Liwan depression (Figure 11). The NW-SE oriented profile provides high-resolution subsurface structural information in the region. As shown in Figure 11b, basement (Tg) is a widespread unconformity that separates the upper sedimentary layer from other layers. At depth of about 9.0 s, a strong continuous reflector extends over the entire length of the profile and can be legibly recognized as reflection Moho. By subtracting the Tg depth from the Moho depth, the crust thickness was estimated to be 2- to 5-s two-way travel time (equivalent to ~4–10 km thick), which is in agreement with our estimated ultrathinning crust thickness. In addition, another approximate 1-s-thick layer (CDP 13348-20000) is observed above the Moho with a very well-defined upper boundary. This 1-s-thick layer prevents the fault cutting down to mantle depth and thus may consist of ductile materials, separating the plastic faulting from the underlying mantle deformation fields (Figure 11b). We note that the numerical results are comparable with the tectonic features of the northern SCS margin: (1) A LVCL remnant remains in the ultrathinning crust when the continent breaks apart in the models; (2) the LVCL lies directly on the Moho, exhibits ductile behavior, and has a rough topography; and (3) large volume sediments deposited in the surface topographic low.

Previous models have assumed that the lower crust is a low-viscosity layer and exhibits a ductile deformation, which leads to the decoupling of the upper and lower lithosphere over a wide area (Huismans & Beaumont, 2011). In their results, the hot, weak lower crust flows toward the spreading center and underplates the areas of localized upper crustal extension. Additionally, the thinning of upper crust is accompanied by little evidence of strong crustal faulting. Our study differs from previous studies, by considering a low-viscosity layer lying between two stronger crustal components, whose existence has been detected in the South China. The weak middle crustal layer flows laterally and exhibit ductile deformation whereas the upper and lower crust is considered to be brittle, because stronger upper and lower crust is chosen in the initial setting of our models. As a result, brittle faults may develop in the upper and lower crust, accumulate large amounts of extension, and form a very thin crust. In the northern SCS margin, the large offset faults are not only recognized in the profile 15eclw8 but also widely exist in other deep reflection seismic profiles. For example, based on a comprehensive tectonosequence analysis of seismic data, it has been suggested that the Baiyun Rift in the northeastern SCS margin is characterized by detachment faults cutting through the continental crust with large offsets (e.g., Dong et al., 2014; Gao et al., 2015; Lei et al., 2019). This detachment fault is a result of lithospheric extension during the rifting the SCS continent (Zhao et al., 2018).

6. Conclusions

Our numerical results present the roles of the LVCL in the development of rifted margin during lithospheric extension. The presence of LVCL mainly controls the width of the highly thinned crust and the crustal thermal distribution. (1) Rheologically weak LVCL accommodates the deformation during extension and thereby delays the thinning of the upper crust. A slow and distributed crustal thinning can be expected when a rheologically weaker and/or thicker LVCL is embedded. (2) Once a weak LVCL exists, the lower crust and lithospheric mantle would be removed before the upper crust, placing the upper crust in direct contact with the hot upwelling asthenosphere. Continuous heating promotes the development of highly thinned continental crust and hot crustal material in the margin. The width of highly thinned crust and crustal thermal value increase when the rheology of the ductile layer decreases or the thickness increases.

Based on our numerical results and gravimetric solutions, we suggested that variation in the LVCL thickness may be a possible mechanism for the differential widths of ultrathinning crust and high heat flow zone along

strike of the northern SCS margin. A thicker LVCL may dominate in the northeastern SCS margin, causing a wider range of ultrathinning crust and high heat flow zone. By contrast, a thinner LVCL exists in the northwestern SCS margin, and thus, a narrower ultra-thinning crust and high heat flow zone can be found in the region.

References

Allken, V., Huismans, R. S., & Thieulot, C. (2012). Factors controlling the mode of rift interaction in brittle-ductile coupled systems: A 3D numerical study. *Geochemistry, Geophysics, Geosystems*, *13*, Q05010. https://doi.org/10.1029/2012GC004077

Bai, Y., Dong, D., Brune, S., Wu, S., & Wang, Z. (2019). Crustal stretching style variations in the northern margin of the South China Sea. *Tectonophysics*, *751*, 1–12.

Barckhausen, U., Engels, M., Franke, D., Ladage, S., & Pubellier, M. (2014). Evolution of the South China Sea: Revised ages for breakup and seafloor spreading. *Marine and Petroleum Geology*, *58*, 599–611. https://doi.org/10.1016/j.marpetgeo.2014.02.022

Becker, J., Sandwell, D., Smith, W., Braud, J., Binder, B., Depner, J., et al. (2009). Global bathymetry and elevation data at 30 arc seconds resolution: SRTM30_PLUS. *Marine Geodesy*, *32*(4), 355–371. https://doi.org/10.1080/01490410903297766

Blanco-Quintero, I. F., Gerya, T. V., García-Casco, A., & Castro, A. (2011). Subduction of young oceanic plates: A numerical study with application to aborted thermal-chemical plumes. *Geochemistry, Geophysics, Geosystems*, *12*, Q10012. https://doi.org/10.1029/2011GC003717

Brune, S., Heine, C., Clift, P. D., & Pérez-Gussinyé, M. (2017). Rifted margin architecture and crustal rheology: Reviewing Iberia-Newfoundland, central South Atlantic, and South China Sea. *Marine and Petroleum Geology*, *79*, 257–281.

Brune, S., Heine, C., Pérezgussinyé, M., & Sobolev, S. V. (2014). Rift migration explains continental margin asymmetry and crustal hyper-extension. *Nature Communications*, *5*(1), 4014. https://doi.org/10.1038/ncomms5014

Burg, J. P., & Gerya, T. (2005). The role of viscous heating in Barrovian metamorphism of collisional orogens: Thermomechanical models and application to the Lepontine Dome in the Central Alps. *Journal of Metamorphic Geology*, *23*(2), 75–95. https://doi.org/10.1111/j.1525-1314.2005.00563.x

Burov, E., & Watts, A. (2006). The long-term strength of continental lithosphere: "Jelly sandwich" or "crème brûlée"? *GSA Today*, *16*(1), 4. https://doi.org/10.1130/1052-5173(2006)016<4:TLTSOC>2.0.CO;2

Chen, L., Hu, J., Yang, D., Song, H., & Wang, Z. (2017). Kinematic models for the opening of the South China Sea: An upwelling divergent flow origin. *Journal of Geodynamics*, *107*, 20–33.

Clerc, C., Lahfid, A., Monié, P., Lagabrielle, Y., Chopin, C., Poujol, M., et al. (2015). High-temperature metamorphism during extreme thinning of the continental crust: A reappraisal of the North Pyrenean passive paleomargin. *Solid Earth*, *6*(2), 643–668. https://doi.org/10.5194/se-6-643-2015

Clift, P., & Lin, J. (2001). Preferential mantle lithospheric extension under the South China margin. *Marine and Petroleum Geology*, *18*(8), 929–945. https://doi.org/10.1016/S0264-8172(01)00037-X

Contrucci, I., Klingelhöfer, F., Perrot, J., Bartolome, R., Gutscher, M.-A., Sahabi, M., et al. (2004). The crustal structure of the NW Moroccan continental margin from wide-angle and reflection seismic data. *Geophysical Journal International*, *159*(1), 117–128.

Crameri, F., Tackley, P., Meilick, I., Gerya, T., & Kaus, B. (2012). A free plate surface and weak oceanic crust produce single-sided subduction on Earth. *Geophysical Research Letters*, *39*, L03306. https://doi.org/10.1029/2011GL050046

Dean, S., Minshull, T., Whitmarsh, R., & Louden, K. (2000). Deep structure of the ocean-continent transition in the southern Iberia Abyssal Plain from seismic refraction profiles: The IAM-9 transect at 40 20′ N. *Journal of Geophysical Research*, *105*(B3), 5859–5885. https://doi.org/10.1029/1999JB900301

Deng, Y. F., Li, S. L., Fan, W. M., & Liu, J. (2011). Crustal structure beneath South China revealed by deep seismic soundings and its dynamics implications. *Chinese Journal of Geophysics*, *54*(10), 2560–2574.

Ding, W., Sun, Z., Dadd, K., Fang, Y., & Li, J. (2018). Structures within the oceanic crust of the central South China Sea basin and their implications for oceanic accretionary processes. *Earth and Planetary Science Letters*, *488*, 115–125. https://doi.org/10.1016/j.epsl.2018.02.011

Dong, D., Wu, S., Li, J., & Lüdmann, T. (2014). Tectonic contrast between the conjugate margins of the South China Sea and the implication for the differential extensional model. *Science China Earth Sciences*, *57*(6), 1415–1426. https://doi.org/10.1007/s11430-013-4740-0

Ducoux, M. (2017). Structure, thermicité et évolution géodynamique de la Zone Interne Métamorphique des Pyrénées. Université d'Orléans.

Duretz, T., Petri, B., Mohn, G., Schmalholz, S., Schenker, F., & Müntener, O. (2016). The importance of structural softening for the evolution and architecture of passive margins. *Scientific Reports*, *6*(1), 38704. https://doi.org/10.1038/srep38704

Fabriès, J., Lorand, J.-P., & Bodinier, J.-L. (1998). Petrogenetic evolution of orogenic lherzolite massifs in the central and western Pyrenees. *Tectonophysics*, *292*(1-2), 145–167. https://doi.org/10.1016/S0040-1951(98)00055-9

Fan, C., Xia, S., Cao, J., Zhao, F., Sun, J., Wan, K., & Xu, H. (2019). Lateral crustal variation and post-rift magmatism in the northeastern South China Sea determined by wide-angle seismic data. *Marine Geology*, *410*, 70–87.

Franke, D., Savva, D., Pubellier, M., Steuer, S., Mouly, B., Auxietre, J.-L., et al. (2014). The final rifting evolution in the South China Sea. *Marine and Petroleum Geology*, *58*, 704–720. https://doi.org/10.1016/j.marpetgeo.2013.11.020

Gao, J., Wu, S., McIntosh, K., Mi, L., Yao, B., Chen, Z., & Jia, L. (2015). The continent–ocean transition at the mid-northern margin of the South China Sea. *Tectonophysics*, *654*, 1–19. https://doi.org/10.1016/j.tecto.2015.03.003

Gerlings, J., Louden, K. E., Minshull, T. A., & Nedimović, M. R. (2012). Flemish Cap–Goban Spur conjugate margins: New evidence of asymmetry. *Geology*, *40*(12), 1107–1110. https://doi.org/10.1130/G33263.1

Gerya, T. (2010). *Introduction to Numerical Geodynamic Modelling*. Cambridge, UK: Cambridge University Press. https://doi.org/10.1017/CBO9780511809101

Gerya, T. V., & Yuen, D. A. (2003). Rayleigh–Taylor instabilities from hydration and melting propel "cold plumes" at subduction zones. *Earth and Planetary Science Letters*, *212*(1-2), 47–62. https://doi.org/10.1016/S0012-821X(03)00265-6

Golberg, J., & Leyreloup, A. (1990). High temperature-low pressure Cretaceous metamorphism related to crustal thinning (Eastern North Pyrenean Zone, France). *Contributions to Mineralogy and Petrology*, *104*(2), 194–207. https://doi.org/10.1007/BF00306443

Gómez-Ortiz, D., & Agarwal, B. N. (2005). 3DINVER. M: A MATLAB program to invert the gravity anomaly over a 3D horizontal density interface by Parker–Oldenburg's algorithm. *Computers & Geosciences*, *31*(4), 513–520. https://doi.org/10.1016/j.cageo.2004.11.004

Gueydan, F., & Précigout, J. (2014). Modes of continental rifting as a function of ductile strain localization in the lithospheric mantle. *Tectonophysics*, *612*, 18–25.

Hartz, E. H., & Podladchikov, Y. Y. (2008). Toasting the jelly sandwich: The effect of shear heating on lithospheric geotherms and strength. *Geology*, *36*(4), 331–334.

He, L., Wang, K., Xiong, L., & Wang, J. (2001). Heat flow and thermal history of the South China Sea. *Physics of the Earth and Planetary Interiors*, *126*(3-4), 211–220. https://doi.org/10.1016/S0031-9201(01)00256-4

Hopper, J., Funck, T., & Tucholke, B. (2007). Structure of the Flemish Cap margin, Newfoundland: insights into mantle and crustal processes during continental breakup. *Geological Society, London, Special Publications*, *282*(1), 47–61. https://doi.org/10.1144/SP282.3

Hu, X. Y., Bi, B. T., Liu, G. X., Han, J. T., Cai, J. C., Peng, R. H., et al. (2017). The lithospheric electrical structure of JI'AN-FUZHOU profile in the east part of South China. *Chinese Journal of Geophysics*, *60*(5), 532–543.

Huang, C.-Y., Yen, Y., Zhao, Q., & Lin, C.-T. (2012). Cenozoic stratigraphy of Taiwan: Window into rifting, stratigraphy and paleoceanography of South China Sea. *Chinese Science Bulletin*, *57*(24), 3130–3149. https://doi.org/10.1007/s11434-012-5349-y

Huismans, R., & Beaumont, C. (2011). Depth-dependent extension, two-stage breakup and cratonic underplating at rifted margins. *Nature*, *473*(7345), 74.

Huismans, R. S., & Beaumont, C. (2014). Rifted continental margins: The case for depth-dependent extension. *Earth and Planetary Science Letters*, *407*, 148–162. https://doi.org/10.1016/j.epsl.2014.09.032

Huismans, R. S., Podladchikov, Y. Y., & Cloetingh, S. (2001). Transition from passive to active rifting: Relative importance of asthenospheric doming and passive extension of the lithosphere. *Journal of Geophysical Research*, *106*(B6), 11,271–11,291. https://doi.org/10.1029/2000JB900424

Jammes, S., Manatschal, G., Lavier, L., & Masini, E. (2009). Tectonosedimentary evolution related to extreme crustal thinning ahead of a propagating ocean: Example of the western Pyrenees. *Tectonics*, *28*, TC4012. https://doi.org/10.1029/2008TC002406

Jian, Z., Larsen, H. C., Alvarez Zarikian, C. A., & the Expedition 368 Scientists (2018). Expedition 368 Preliminary Report: South China Sea Rifted Margin. *International Ocean Discovery Program*. https://doi.org/10.14379/iodp.pr.368.2018

Kendall, R., Mitrovica, J., & Sabadini, R. (2003). Lithospheric thickness inferred from Australian post-glacial sea-level change: The influence of a ductile crustal zone. *Geophysical Research Letters*, *30*(9), 1461. https://doi.org/10.1029/2003GL017022

Klepeis, K. A., King, D., de Paoli, M., Clarke, G. L., & Gehrels, G. (2007). Interaction of strong lower and weak middle crust during lithospheric extension in western New Zealand. *Tectonics*, *26*, TC4017. https://doi.org/10.1029/2006TC002003

Kuo-Chen, H., Wu, F., Jenkins, D., Mechie, J., Roecker, S., Wang, C. Y., & Huang, B. S. (2012). Seismic evidence for the α-β quartz transition beneath Taiwan from Vp/Vs tomography. *Geophysical Research Letters*, *39*, TC4017. https://doi.org/10.1029/2012GL053649

Lagabrielle, Y., & Bodinier, J. L. (2008). Submarine reworking of exhumed subcontinental mantle rocks: field evidence from the Lherz peridotites, French Pyrenees. *Terra Nova*, *20*(1), 11–21. https://doi.org/10.1111/j.1365-3121.2007.00781.x

Larsen, H. C., Mohn, G., Nirrengarten, M., Sun, Z., Stock, J., Jian, Z., et al. (2018). Rapid transition from continental breakup to igneous oceanic crust in the South China Sea. *Nature Geoscience*, *11*(10), 782.

Lau, K. H., Louden, K. E., Deemer, S., Hall, J., Hopper, J. R., Tucholke, B. E., et al. (2006). Crustal structure across the Grand Banks—Newfoundland Basin Continental Margin—II. Results from a seismic reflection profile. *Geophysical Journal International*, *167*(1), 157–170.

Lau, K. H., Nedimović, M. R., & Louden, K. E. (2018). Continent-ocean transition across the northeastern Nova Scotian margin from a dense wide-angle seismic profile. *Journal of Geophysical Research: Solid Earth*, *123*, 4331–4359. https://doi.org/10.1029/2017JB015282

Lavier, L. L., & Manatschal, G. (2006). A mechanism to thin the continental lithosphere at magma-poor margins. *Nature*, *440*(7082), 324–328. https://doi.org/10.1038/nature04608

Le Pourhiet, L., Chamot-Rooke, N., Delescluse, M., May, D. A., Watremez, L., & Pubellier, M. (2018). Continental break-up of the South China Sea stalled by far-field compression. *Nature Geoscience*, *11*(8)–605.

Lei, C., Alves, T. M., Ren, J., Pang, X., Yang, L., & Liu, J. (2019). Depositional architecture and structural evolution of a region immediately inboard of the locus of continental breakup (Liwan Sub-basin, South China Sea). *Geological Society of America Bulletin*. https://doi.org/10.1130/B35001.1

Lei, X. (2013). *Studies on the Heat Flow and Thermo-Mechanism of the Lithosphere in the Northern South China Sea Margin*, (pp. 1–5). Nanjing: Nanjing University.

Lenardic, A., Moresi, L.-N., Jellinek, A., & Manga, M. (2005). Continental insulation, mantle cooling, and the surface area of oceans and continents. *Earth and Planetary Science Letters*, *234*(3-4), 317–333. https://doi.org/10.1016/j.epsl.2005.01.038

Li, F., Sun, Z., & Yang, H. (2018). Possible Spatial Distribution of the Mesozoic Volcanic Arc in the Present-Day South China Sea Continental Margin and Its Tectonic Implications. *Journal of Geophysical Research: Solid Earth*, *123*(8), 6215–6235.

Li, F., Sun, Z., & Zhang, J. (2018). Influence of mid-crustal rheology on the deformation behavior of continental crust in the continental subduction zone. *Journal of Geodynamics*, *117*, 88–99. https://doi.org/10.1016/j.jog.2018.04.002

Li, X.-H., Li, Z.-X., Li, W.-X., Liu, Y., Yuan, C., Wei, G., & Qi, C. (2007). U–Pb zircon, geochemical and Sr–Nd–Hf isotopic constraints on age and origin of Jurassic I-and A-type granites from central Guangdong, SE China: a major igneous event in response to foundering of a subducted flat-slab? *Lithos*, *96*(1-2), 186–204. https://doi.org/10.1016/j.lithos.2006.09.018

Liao, J., & Gerya, T. (2014). Influence of lithospheric mantle stratification on craton extension: Insight from two-dimensional thermomechanical modeling. *Tectonophysics*, *631*, 50–64. https://doi.org/10.1016/j.tecto.2014.01.020

Liao, J., & Gerya, T. (2015). From continental rifting to seafloor spreading: insight from 3D thermo-mechanical modeling. *Gondwana Research*, *28*(4), 1329–1343. https://doi.org/10.1016/j.gr.2014.11.004

Liao, Q. L., Wang, Z. M., Wang, P. L., Yu, Z. K., Wu, N. Y., & Liu, B. C. (1988). Explosion seismic study of the crustal structure in Fuzhou-Quanzhou-Shantou region [in Chinese with English abstract]. *Chinese Journal of Geophysics*, *3*, 270–280.

Lin, C. T., Harris, R., Sun, W. D., & Zhang, G. L. (2019). Geochemical and Geochronological Constraints on the Origin and Emplacement of the East Taiwan Ophiolite. *Geochemistry, Geophysics, Geosystems*.

Liu, Z., Zhao, H., & Fan, S. (2002). *Geology of the South China Sea*. Beijing: Science Press.

Lü, C. C., Hao, T. Y., Qiu, X. L., & Zhao, M. H. (2011). A study on the deep structure of the northern part of southwest sub-basin from ocean bottom seismic data, South China Sea [in Chinese with English abstract]. *Chinese Journal of Geophysics*, *54*(12), 3129–3138.

Mao, J. R., Tao, K. Y., Xing, G. F., Yang, Z. L., & Zhao, Y. (1999). Petrological records of the Mesozoic-Cenozoic mantle plume tectonics in epincontinental area of Southeast China [in Chinese with English abstract]. *Acta Geoscientia Sinica*, *20*(3), 253–258.

Masini, E., Manatschal, G., Tugend, J., Mohn, G., & Flament, J.-M. (2014). The tectono-sedimentary evolution of a hyper-extended rift basin: The example of the Arzacq–Mauléon rift system (Western Pyrenees, SW France). *International Journal of Earth Sciences*, *103*(6), 1569–1596. https://doi.org/10.1007/s00531-014-1023-8

McIntosh, K., Nakamura, Y., Wang, T. K., Shih, R. C., Chen, A., & Liu, C. S. (2005). Crustal-scale seismic profiles across Taiwan and the western Philippine Sea. *Tectonophysics*, *401*(1-2), 23–54. https://doi.org/10.1016/j.tecto.2005.02.015

Mechie, J., Yuan, X., Schurr, B., Schneider, F., Sippl, C., Ratschbacher, L., et al. (2012). Crustal and uppermost mantle velocity structure along a profile across the Pamir and southern Tien Shan as derived from project TIPAGE wide-angle seismic data. *Geophysical Journal International*, *188*(2), 385–407. https://doi.org/10.1111/j.1365-246X.2011.05278.x

Mi, L., Yuan, Y., & Zhang, G. (2009). Characteristics and genesis of geothermal field in deep-water area of the northern South China Sea [in Chinese with English abstract]. *Acta Petrolei Sinica*, *30*(1), 27–32.

Morley, C. (2016). Major unconformities/termination of extension events and associated surfaces in the South China Seas: Review and implications for tectonic development. *Journal of Asian Earth Sciences*, *120*, 62–86. https://doi.org/10.1016/j.jseaes.2016.01.013

Oldenburg, D. W. (1974). The inversion and interpretation of gravity anomalies. *Geophysics*, *39*(4), 526–536. https://doi.org/10.1190/1.1440444

Parker, R. (1973). The rapid calculation of potential anomalies. *Geophysical Journal International*, *31*(4), 447–455. https://doi.org/10.1111/j.1365-246X.1973.tb06513.x

Pérez-Gussinyé, M., Morgan, J. P., Reston, T. J., & Ranero, C. R. (2006). The rift to drift transition at non-volcanic margins: Insights from numerical modelling. *Earth and Planetary Science Letters*, *244*(1–2), 458–473. https://doi.org/10.1016/j.epsl.2006.01.059

Pérez-Gussinyé, M., Ranero, C. R., Reston, T. J., & Sawyer, D. (2003). Mechanisms of extension at nonvolcanic margins: Evidence from the Galicia interior basin, west of Iberia. *Journal of Geophysical Research*, *108*(B5), 2245. https://doi.org/10.1029/2001JB000901

Peron-Pinvidic, G., Manatschal, G., & Osmundsen, P. T. (2013). Structural comparison of archetypal Atlantic rifted margins: A review of observations and concepts. *Marine and Petroleum Geology*, *43*, 21–47. https://doi.org/10.1016/j.marpetgeo.2013.02.002

Pichot, T., Delescluse, M., Chamot-Rooke, N., Pubellier, M., Qiu, Y., Meresse, F., et al. (2014). Deep crustal structure of the conjugate margins of the SW South China Sea from wide-angle refraction seismic data. *Marine and Petroleum Geology*, *58*, 627–643. https://doi.org/10.1016/j.marpetgeo.2013.10.008

Prada, M., Watremez, L., Chen, C., O'Reilly, B. M., Minshull, T. A., Reston, T. J., et al. (2017). Crustal strain-dependent serpentinisation in the Porcupine Basin, offshore Ireland. *Earth and Planetary Science Letters*, *474*, 148–159. https://doi.org/10.1016/j.epsl.2017.06.040

Qiu, X., Ye, S., Wu, S., Shi, X., Zhou, D., Xia, K., & Flueh, E. R. (2001). Crustal structure across the Xisha trough, northwestern South China Sea. *Tectonophysics*, *341*(1–4), 179–193.

Qin, J. X., Hao, T. Y., Xu, Y., Huang, S., Lu, C. C., & Hu, W. J. (2011). The distribution characteristics and the relationship between the tectonic units of the Moho depth in South China Sea and adjacent areas. *Diqiu Wuli Xuebao*, *54*(12), 3171–3183.

Qiu, Y., & Chen, G. N. (2011). Mechanism of the Cenozoic tecto-geomorphologic evolution in the Southeast China continental margin [in Chinese with English abstract]. *Earth Science Frontiers*, *18*(1), 032–038.

Ranalli, G. (1995). *Rheology of the Earth*. Berlin: Springer Science & Business Media.

Ranero, C. R., & Pérez-Gussinyé, M. (2010). Sequential faulting explains the asymmetry and extension discrepancy of conjugate margins. *Nature*, *468*(7321), 294–299. https://doi.org/10.1038/nature09520

Ros, E., Pérez Gussinyé, M., Araujo, M., Romeiro, M. T., Andres Artinez, M., & Morgan, J. P. (2017). Lower crustal strength controls on melting and serpentinization at magma margins: Potential implications for the South Atlantic. *Geochemistry, Geophysics, Geosystems*, *18*, 4538–4557. https://doi.org/10.1002/2017GC007212

Ruan, A. G., Niu, X. W., Qiu, X. L., Li, J. B., Wu, Z. L., Zhao, M. H., & Wei, X. D. (2011). A wide angle ocean bottom seismometer experiment across Liyue Bank, the southern margin of the South China Sea. *Chinese Journal of Geophysics*, *54*(54), 3139–3149.

Sandwell, D. T., Müller, R. D., Smith, W. H., Garcia, E., & Francis, R. (2014). New global marine gravity model from CryoSat-2 and Jason-1 reveals buried tectonic structure. *Science*, *346*(6205), 65–67. https://doi.org/10.1126/science.1258213

Schmeling, H., Babeyko, A., Enns, A., Faccenna, C., Funiciello, F., Gerya, T., et al. (2008). A benchmark comparison of spontaneous subduction models—Towards a free surface. *Physics of the Earth and Planetary Interiors*, *171*(1-4), 198–223. https://doi.org/10.1016/j.pepi.2008.06.028

Shi, X., Qiu, X., Xia, K., & Zhou, D. (2003). Characteristics of surface heat flow in the South China Sea. *Journal of Asian Earth Sciences*, *22*(3), 265–277. https://doi.org/10.1016/S1367-9120(03)00059-2

Shi, X. B., Yu, C. H., Chen, M., Yang, X. Q., & Zhao, J. F. (2017). Analyses of variation features and influential factors of heat flow in the northern margin of the South China Sea [in Chinese with English abstract]. *Earth Science Frontiers*, *24*(3), 56–64.

Sibuet, J. C., & Hsu, S. K. (1997). Geodynamics of the Taiwan arc-arc collision. *Tectonophysics*, *274*(1-3), 221–251. https://doi.org/10.1016/S0040-1951(96)00305-8

Sibuet, J. C., Srivastava, S. P., & Spakman, W. (2004). Pyrenean orogeny and plate kinematics. *Journal of Geophysical Research*, *109*, B08104. https://doi.org/10.1029/2003JB002514

Sun, Z., Stock, J., Klaus, A., and the Expedition 367 Scientists (2018). Expedition 367 preliminary report: South China Sea rifted margin. International Ocean Discovery Program. https://doi.org/10.14379/iodp.pr.367.2018

Sun, Z., Zhao, Z. X., Li, J. B., Zhou, D., & Wang, Z. W. (2011). Tectonic analysis of the breakup and bollision unconformities in the Nansha Block. *Chinese Journal of Geophysics*, *54*(6), 1069–1083. https://doi.org/10.1002/cjg2.1685

Svartman Dias, A. E., Lavier, L. L., & Hayman, N. W. (2015). Conjugate rifted margins width and asymmetry: The interplay between lithospheric strength and thermomechanical processes. *Journal of Geophysical Research: Solid Earth*, *120*, 8672–8700. https://doi.org/10.1002/2015JB012074

Tapponnier, P., Lacassin, R., Leloup, P. H., Schärer, U., Dalai, Z., Haiwei, W., et al. (1990). The Ailao Shan/Red River metamorphic belt: Tertiary left-lateral shear between Indochina and South China. *Nature*, *343*(6257), 431–437. https://doi.org/10.1038/343431a0

Tetreault, J. L., & Buiter, S. J. H. (2017). The influence of extension rate and crustal rheology on the evolution of passive margins from rifting to break-up. *Tectonophysics*, *106*, 3961–3975. https://doi.org/10.1029/2000JB900325

Tsai, C.-H., Hsu, S.-K., Yeh, Y.-C., Lee, C.-S., & Xia, K. (2004). Crustal thinning of the northern continental margin of the South China Sea. *Marine Geophysical Researches*, *25*(1-2), 63–78. https://doi.org/10.1007/s11001-005-0733-5

Turcotte, D., & Schubert, G. (2014). *Geodynamics*. Cambridge University Press. https://doi.org/10.1017/CBO9780511843877

Unsworth, M., Jones, A. G., Wei, W., Marquis, G., Gokarn, S., Spratt, J., et al. (2005). Crustal rheology of the Himalaya and Southern Tibet inferred from magnetotelluric data. *Nature*, *438*(7064), 78–81. https://doi.org/10.1038/nature04154

Vacherat, A., Mouthereau, F., Pik, R., Bernet, M., Gautheron, C., Masini, E., et al. (2014). Thermal imprint of rift-related processes in orogens as recorded in the Pyrenees. *Earth and Planetary Science Letters*, *408*, 296–306. https://doi.org/10.1016/j.epsl.2014.10.014

Vauchez, A., Clerc, C., Bestani, L., Lagabrielle, Y., Chauvet, A., Lahfid, A., & Mainprice, D. (2013). Preorogenic exhumation of the North Pyrenean Agly massif (Eastern Pyrenees-France). *Tectonics*, *32*, 95–106. https://doi.org/10.1002/tect.20015

Vink, G. E. (1982). Continental rifting and the implications for plate tectonic reconstructions. *Journal of Geophysical Research*, *87*(B13), 10,677–10,688. https://doi.org/10.1029/JB087iB13p10677

Wang, T. K., Chen, M.-K., Lee, C.-S., & Xia, K. (2006). Seismic imaging of the transitional crust across the northeastern margin of the South China Sea. *Tectonophysics*, *412*(3-4), 237–254. https://doi.org/10.1016/j.tecto.2005.10.039

Wei, X. D., Ruan, A. G., Zhao, M. H., Qiu, X. L., Li, J. B., Zhu, J. J., et al. (2011). A Wide-Angle Obs Profile Across the Dongsha Uplift and Chaoshan Depression in the Mid-Northern South China Sea [in Chinese with English abstract]. *Chinese Journal of Geophysics*, *54*(6), 3325–3335.

Whitmarsh, R., Manatschal, G., & Minshull, T. (2001). Evolution of magma-poor continental margins from rifting to seafloor spreading. *Nature*, *413*(6852), 150–154. https://doi.org/10.1038/35093085

Whittaker, J. M., Goncharov, A., Williams, S. E., Müller, R. D., & Leitchenkov, G. (2013). Global sediment thickness data set updated for the Australian-Antarctic Southern Ocean. *Geochemistry, Geophysics, Geosystems*, *14*, 3297–3305. https://doi.org/10.1002/ggge.20181

Xu, X., Shi, X., & Luo, X. (2006). Heat flow measurements in the Xisha trough of the South China Sea [in Chinese with English abstract]. *Marine Geology and Quaternary Geology*, *26*(4), 51–58.

Xu, X., Wang, X., Peng, D., Yao, Y., Yao, B., & Wan, Z. (2018). Characteristics and research of heat flow in the northwest sub-basin and its adjacent areas of the South China Sea [in Chinese with English abstract]. *Earth Science*, *43*(10), 3391–3398.

Yan, P., Zhou, D., & Liu, Z. (2001). A crustal structure profile across the northern continental margin of the South China Sea. *Tectonophysics*, *338*(1) 1–21.

Yao, B. C. (1998). Crust structure of the northern margin of the South China Sea and its tectonic significance [in Chinese with English abstract]. *Marine Geology & Quaternary Geology*, *18*(2), 1–16.

Yeh, Y.-C., & Hsu, S.-K. (2004). Crustal structures of the northernmost South China Sea: Seismic reflection and gravity modeling. *Marine Geophysical Researches*, *25*(1-2), 45–61. https://doi.org/10.1007/s11001-005-0732-6

Yeh, Y. C., Sibuet, J. C., Hsu, S. K., & Liu, C. S. (2010). Tectonic evolution of the Northeastern South China Sea from seismic interpretation. *Journal of Geophysical Research*, *115*, B06103. https://doi.org/10.1029/2009JB006354

Yuan, Y., Zhu, W., Mi, L., Zhang, G., Hu, S., & He, L. (2009). "Uniform geothermal gradient" and heat flow in the Qiongdongnan and Pearl River Mouth Basins of the South China Sea. *Marine and Petroleum Geology*, *26*(7), 1152–1162.

Zhang, J., & Wang, J. (2000). The deep thermal characteristic of continental margin of the northern South China Sea. *Chinese Science Bulletin*, *45*(18), 1717–1722. https://doi.org/10.1007/BF02898994

Zhang, Z., & Wang, Y. (2007). Crustal structure and contact relationship revealed from deep seismic sounding data in South China. *Physics of the Earth and Planetary Interiors*, *165*(1-2), 114–126. https://doi.org/10.1016/j.pepi.2007.08.005

Zhao, Y., Ren, J., Pang, X., Yang, L., & Zheng, J. (2018). Structural style, formation of low angle normal fault and its controls on the evolution of Baiyun Rift, northern margin of the South China Sea. *Marine and Petroleum Geology*, *89*, 687–700. https://doi.org/10.1016/j.marpetgeo.2017.11.001